2010-12-16

EIT, Slow light, and Sealing Methods for Embedding Rubidium into the ARROW System

Katherine Barnett Hurd
Brigham Young University - Provo

EIT, Slow light, and Sealing Methods for Embedding

Rubidium into the ARROW System

Katherine Barnett Hurd

A thesis submitted to the faculty of
Brigham Young University
in partial fulfillment of the requirements for the degree of

Master of Science

Aaron R. Hawkins, Chair
Stephen M. Schultz
Richard H. Selfridge

Department of Electrical and Computer Engineering

Brigham Young University

April 2011

ABSTRACT

EIT, Slow light, and Sealing Methods for Embedding

Rubidium into the ARROW System

Katherine Barnett Hurd

Department of Electrical and Computer Engineering

Master of Science

Light-matter interactions are fundamentally based on the quantum mechanical principles that govern photons, electrons and other fundamental particles. One very interesting phenomenon within all of light-matter interactions is Electromagnetically Induced Transparency (EIT). This phenomenon causes an otherwise absorbing atomic transition to stop absorbing through quantum mechanical interference of probability wave functions. Corresponding to that change in absorption, will be a sudden, large change in the index of refraction. This change in the index of refraction leads to another phenomenon in which the group velocity of light can be slowed down dramatically.

In the past, many researchers have been able to achieve both EIT and slow light in bulk atomic vapor cells. In an attempt to miniaturize this process and we have been using a platform of Anti Resonant Reflecting Optical Waveguides (ARROW) devices to both guide light and contain the interacting matter. However, the platform creates a whole new set of challenges when integrating rubidium vapor into the hollow waveguides as rubidium is highly reactive and it is difficult to maintain an inert atmosphere for the rubidium vapor.

A variety of sealing methods were attempted and their appropriateness and effectiveness was analyzed. Among these sealing methods were PMMA, Crystal Wax, Active Solder, Epoxy, and Indium Solder. PMMA, Crystal Wax and Active Solder each had major faults in one or more of the sealing requirements. We have used a high temperature epoxy with relative success to contain the rubidium vapor. However, the epoxy degrades very quickly at the high temperatures required for EIT testing. Indium solder is the most recent application method. It has high potential although we have yet to fully test its effectiveness.

We were able to successfully demonstrate the first EIT and slow light on a chip with our ARROW atomic vapor cell system. In the slow light experiment, we were able to slow light down to 2.5×10^5 m/s. The group velocity of light decreased from the standard 3×10^8 m/s by a factor of 1200. We believe we can achieve even lower group velocities using this same platform through further experimentation.

Keywords: EIT, slow light, rubidium reactance, atomic vapor cells

ACKNOWLEDGEMENTS

I'd like to thank my advisor Dr Hawkins for his unfailing support of me and for giving me the opportunities that were necessary for me to get to this point in my graduate career. He has been an invaluable advisor. Additionally, John Hulbert and Bin Wu have been wonderful and have done so much work on this project that I have been able to use.

Particularly, my wonderful figure guy, caterer, receiver of rants, co-conspirator and best husband ever has been my pillar and has pulled me through so many of those hard days that I didn't how to progress forward.

My family, particularly my father has provided much needed sounding board aid and encouragement in this particular endeavor.

As I started doing research on EIT and slow light I was surprised at just how much I didn't understand. I somehow thought that my two semesters of quantum mechanics my senior year of my undergraduate degree combined with my go-getter attitude would magically transform any complicated scientific paper into something easily understood. Clearly, it was a bit of shock to me that even after re-reading multiple times, and with many reference resources, the papers on EIT and slow light were next to unintelligible. There were so many concepts that I did not understand. I couldn't even follow to the authors in their basic assumptions.

Often authors of such papers don't even bother to explain the true roots of their derivations or what exactly is going on. They have no reason to because they are writing scientific papers, which are meant to be as concise as possible, so very specific terminology is

used as well as prederived equations. This is great for much of their audience, but for those of us just breaking into the field, it is difficult.

This is one of the main driving forces behind the style in this thesis. I have tried to take many of the concepts that come up often in EIT, slow light, and other quantum coherence papers and trace them back to their simplest roots. This has allowed me to have a more thorough understanding of what exactly is going on, and will hopefully help anyone who happens to read this to be able to have an easier transition into the world of quantum optical coherence.

My other goal of this thesis is to have a thorough explanation of the packaging experiments, so that anyone joining the research group will be able to replicate my work. I will be successful if this person has a shallower learning curve and he or she is able to jump in and pick up right where I left off, and if that person avoids a long period of time in which nothing gets done while he or she learns the ropes. My hope is that this can act as a handbook for them in all things EIT, slow light, sealing and packaging.

TABLE OF CONTENTS

LIST OF FIGURES

1. Introduction

Light is quantized. Electromagnetic radiation is quantized. All matter is quantized. In this way we live in a quantum world. However these quantized pieces of the world are very small and any quantum interactions are so minute that we as human beings rarely if ever see these quantum interactions or realize that the quantized pieces are there and that they are important. As technology progresses and becomes more complicated, many scientists are researching various quantum processes and looking for ways to harness these effects to achieve certain ends. Electromagnetically Induced Transparency (EIT) is an example of a quantum optic effect that is receiving attention and could potentially be harnessed for a variety of purposes.

1.1. History of EIT and Slow Light

The physical effect behind EIT is called coherent population trapping. Gerardo, et al, discovered it in 1976. They were able to show that under the proper conditions, when the spacing of the modes of a multimode laser matched up with hyperfine states in sodium, they were able to drive the probability amplitudes into a superposition of two states and leave a third state empty, thus reducing the fluorescence from the third state [1]. This was followed up in 1986 by Kocharovskaya et al who showed that this was also possible to achieve in a dense medium using two lasers of different frequencies [1][3]. This previous work was harnessed by Stephen Harris and simultaneously by Kocharovskaya and Khanin (working together) and followed by

others who postulated different techniques to use this coherent population trapping phenomenon to create lasers without the need for population inversion [4][5][6][7].

Later Harris and colleagues were able to demonstrate Electromagnetically Induced Transparency (EIT), a term that Harris himself coined in optically opaque strontium vapor [8][9]. Since then EIT has been observed in multiple substances and under multiple experimental conditions. A few good reviews of Electromagnetically Induced Transparency are listed in the reference section of this thesis [10][11][12].

When EIT occurs, the refractive properties of a medium simultaneously undergo significant changes and these media can have very unusual optical properties. These optical properties can lead to creating slow light [13] (i.e. reducing the group velocity v_g of a propagating light beam) among other phenomena.

Slow light ultimately is due to manipulation of the frequency dependence of the refractive index. In addition to EIT resonances [14][15][16], other phenomena and methods have been used to slow down light. These include coherent population oscillations [13], atomic double resonances [17], photonic crystal waveguides [18][19][20][21] coupled resonator optical waveguides (CROWs) [22], and stimulated Brillouin scattering (SBS) in optical fiber [23]. Many of these methods, however, require complicated setups and/or ultra-low temperatures, which makes them difficult to use in applications such as optical buffers, data storage, and as quantum communication devices.

In addition to slow light, EIT can also be utilized to harness typically small nonlinear processes in highly efficient ways including Giant Kerr nonlinearities [24], in low-light purely-

optical switching [25][26][27], storage and retrieval of optical pulses [28], and transverse images [29].

In order to take advantage of these quantum optic phenomena and move away from the complicated set ups in favor of more integratable, practical to use platforms, there has been significant research into slow light and EIT in alternate platforms including optical fibers [30] and photonic crystal fibers [31][32]. Our group has focused on a particular hollow waveguide platform called an ARROW that we load with Rubidium vapor. Using this particular device we have been able to successfully do atomic spectroscopy of Rubidium vapor on a chip [33] and then most recently have been able to successfully perform the first on chip EIT and slow light experiments [34].

1.2. Bulk Rubidium Atomic Vapor Cells

In the past, the only option for Rubidium Atomic vapor cells has been bulky glass blown cells. These cells are coated on the inside with paraffin to keep the atoms from bouncing off the sides of the cells and becoming decoherent [35].

The cells themselves are made from a complicated glass blowing process that can be quite expensive and time consuming. Additionally, Figure 1-1 shows that the cells themselves are quite large, and that the optics and analytic equipment required for operation can fill up an entire optical table.

To be commercially viable, these atomic vapor cells must be miniaturized. It would be very difficult to integrate the large bulk cells into commercial devices that could utilize EIT or slow light in their operation. This thesis addresses a novel approach to Atomic Vapor Cells that

would take large steps toward making them integratable into commercial devices using the ARROW platform.
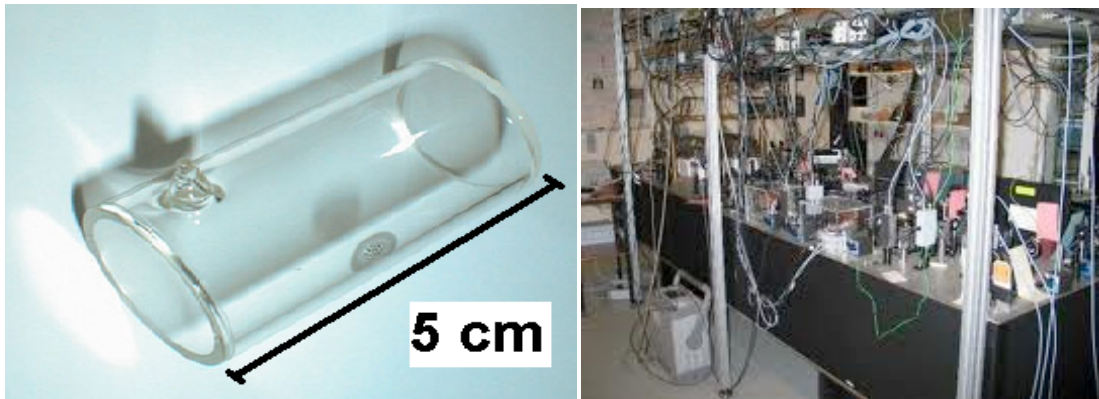
Figure 1-1: The left image shows a sample bulk vapor cell made from Pyrex. The right image shows the optical table and setup required for measuring and analyzing results from bulk atomic vapor cells.

This is not a problem that only is being researched here at Brigham Young University; there are other groups around the world that are investing time into this particular issue. Of particular note are some work being done into anodic bonding at NIST, and into using photonic crystal fibers as atomic vapor cells.

1.3. NIST Rubidium Atomic Vapor Cell

The National Institute of Standards and Technology in Boulder, Colorado has a group that has been working on incorporating Rubidium into super precise atomic clocks. Part of their

research has focused on miniaturizing atomic vapor cells for use in these atomic clocks. As a result, they have made devices that look like Figure 1-2:

This device is manufactured with a silicon wafer that has a hole etched through it. Glass wafers are then bonded to the top and bottom of the silicon wafer with rubidium vapor between them. The attachment between the glass wafers and the chip is done through anodic bonding.
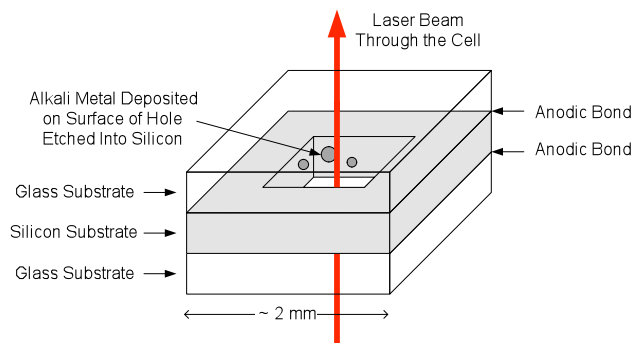
Figure 1-2 Schematic of the vapor cell made by NIST. Created by anodically bonding a silicon wafer between two glass wafers

Although significantly smaller than the bulk cells, the device is still quite large, especially with all the electronics that are associated with it and it still is fairly three-dimensional, as shown in Figure 1-3 [36]. We would like to make a cell that is more two dimensional for monolithic production and integration, this will be made possible through the use of waveguides fabricated directly onto a silicon substrate
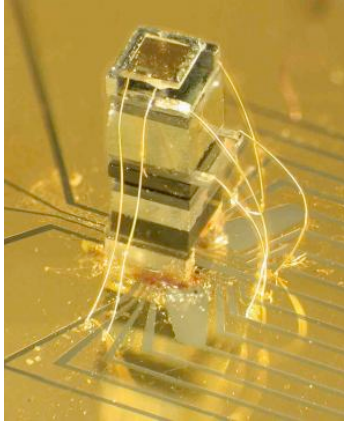
Figure 1-3 Three dimensional nature of the NIST vapor cell

In addition to their first atomic cell, the NIST team has since come out with two new designs that have interesting features. The first, which is shown in Figure 1-4, employs thin film Bragg reflectors on angled walls within the atomic cell. The angled walls reflect the laser beam from a vertical cavity surface emitting laser (VCSEL) through the atomic vapor and back down to the surface of the chip [37].
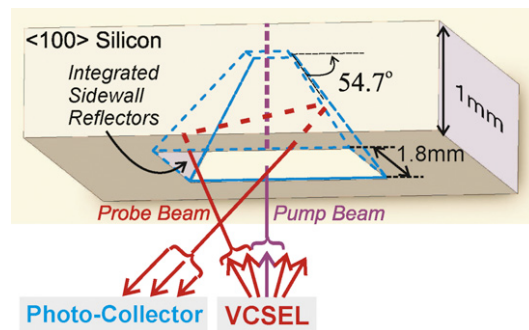
Figure 1-4 NIST vapor cell with Bragg sidewall reflectors. The cell was sealed via anodic bonding

Another version of the NIST vapor cell adds an additional micro-glass-blowing technique. Figure 1-5 from their 2009 publication details the procedure [38].

This recent NIST procedure definitely has some advantages. Namely that it is more planar than the previous NIST iteration, and possibly could be done monolithically. However, their procedure still has the disadvantages that anodic bonding is very difficult to do successfully, and that the bonding must occur at 860°C, a temperature that few materials and structures can withstand.
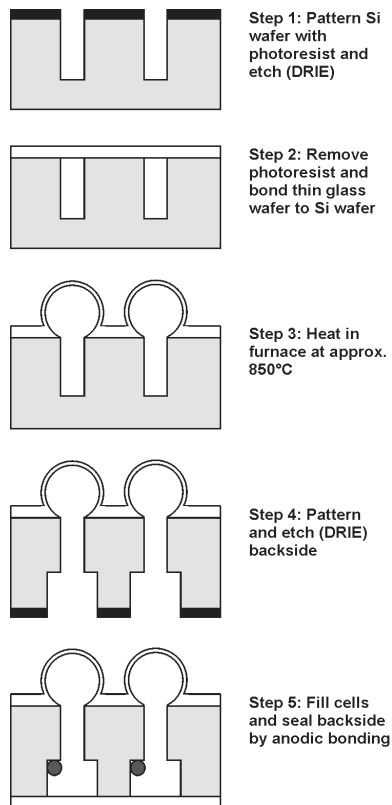
Figure 1-5 NIST procedure for making micro glass blown vapor cells. Cells were sealed with anodic bonding.

1.4. Photonic Crystal Fiber

Another option that has been explored is to use photonic crystal fibers with Rubidium Gas inside them.   Photonic crystal fibers are able to guide light within a mostly gas core because of the specifically arranged chambers within the fiber, which is shown in Figure 1-6. These are wonderful in that they can be coupled to basic fibers easily, and thus allow good propagation of light through the Rubidium gas.   However, as Figure 1-7 shows, these fibers still require an elaborate set up in order to populate the device with Rubidium gas.
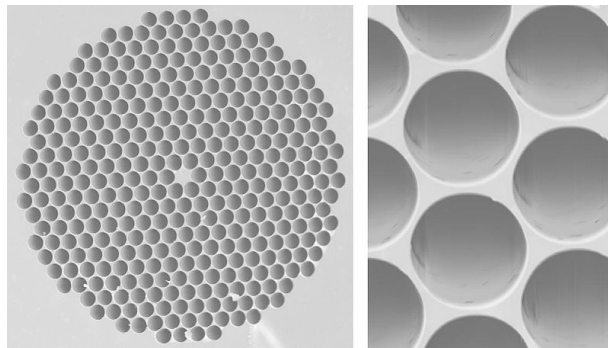
Figure 1-6 Interior view of a sample photonic crystal fiber. Hollow cavities are clearly visible

Many useful experiments have been performed on these types of devices including, but not limited to EIT and slow light [39][21]. This is definitely a viable option in the search for effective miniaturized atomic vapor cells.

1.5. Hollow Core Waveguide Atomic Vapor Cells

We have taken a slightly different approach to this challenge of creating an integratable miniaturized Atomic Vapor Cell for Rubidium vapor. We have created hollow core waveguides into which we load Rubidium vapor. The hollow core waveguides will guide light directly through the Rubidium vapor.   We believe our approach has a few distinct advantages as compared to other approaches. Among them are the following:
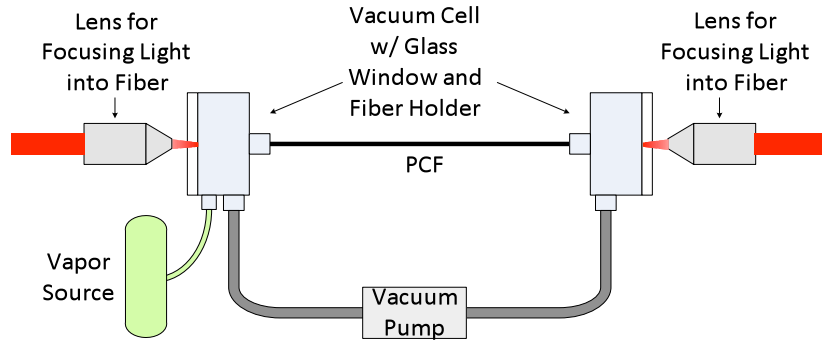
Figure 1-7 Setup required for filling photonic crystal fiber with Rubidium gas.

1) Waveguides allow for long interaction lengths between the laser and the gas. In a standard bulk vapor cell, the interaction length is limited to the region right around the beam waist, which is created by the focusing of the beam due to lenses around the vapor cell. In general in a waveguide-based system, there will be a larger interaction volume than a bulk vapor cell based system. This is illustrated in Figure 1-8.
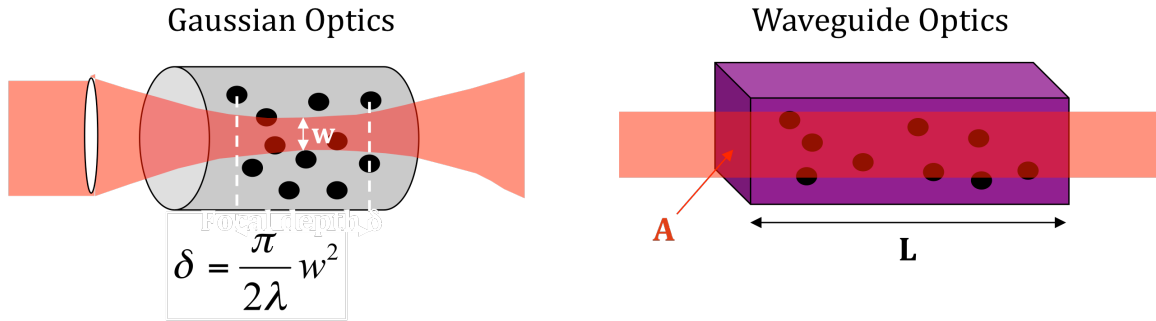
Figure 1-8 Interaction area comparison between Gaussian Optics and Waveguide Optics

2) Our devices could be produced and integrated into other optical devices relatively easily because of their planar nature and because they're built directly on silicon wafers.

3) Our devices could potentially be quite inexpensive. We use standard semiconductor processing techniques, which can be ramped up to large scale processes and consequently bring the cost per unit down substantially.

1.6. ARROW Devices

Total internal reflection is used to contain light and to guide it where we need it to go. Glass optical fibers as well as many waveguides use this mechanism for guiding light. But in order for total internal reflection to occur, the guiding material must have a higher index of refraction than the surrounding material. We see this from the basic Snell's Law:

$$\theta_c = \arcsin\left(\frac{n_2}{n_1}\right)$$

(1)

.

This is the equation for the critical angle, or the incident angle at which the propagating beam of light will entirely reflect without some of the beam being refracted across the interface. As the equation is studied, it is clear to see that in order for this to be a real number n_2 must be larger than n_1. Therefore in order for total internal reflection to occur, the beam must be traveling inside a substance with a higher index of refraction than the surrounding material.

This physical property of total internal reflection makes it ideal for fiber optics, and because of it there's a whole fiber optic communications system that has changed the way the world works. However, often we want to contain light to study fluids or gases, or atoms/molecules within fluids or gases. And here's the problem. Most fluids or gases have a lower or essentially equivalent index of refraction to the surrounding atmosphere. In order to accomplish this, we need to turn to alternative solutions.

One solution is by using dielectric stacks, which are often called Bragg mirrors. Using alternating dielectric layers of specified thicknesses, we can create a situation where there is deconstructive interference on one side of the stack and constructive interference on the other. So, even though the index of refraction on either side of the dielectric mirror is the same, and total internal relection will not occur, the dielectric mirror reflects all or most of the light very similarly to light reflected in total internal reflection.

The ARROW (Anti Resonant Reflecting Optical Waveguides) structures created here at BYU [41][42] take advantage of these dielectric stacks to create hollow and liquid-core waveguides using typical semiconductor processing techniques. These waveguides have dielectric mirrors surrounding a gas or liquid filled core, so the propagating light beam is

contained and we are able to analyze and look at interactions between the light and whatever is

contained within the core. These dielectric mirrors are illustrated in Figure 1-9.
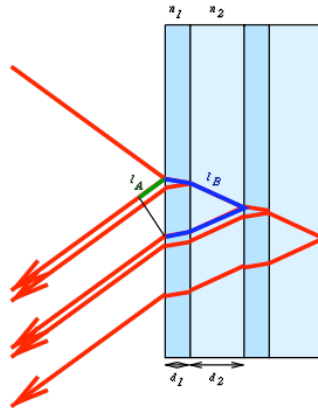
Figure 1-9 Dielectric mirror

Ultimately, the waveguides should look something like what is shown in Figure 1-10, with a core of a low index, and dielectric stacks on the top, bottom, and sides of the waveguide.

The variable that determines whether this waveguide will actually guide light or not is the thickness of each of the dielectric layers. This is dependent on the wavelength of light to be guided, the thickness of the core (d_c), as well as the indices of refraction for the core (n_c) and the dielectric layers (n_j). The thicknesses are determined by the equation,

$$t_j = \frac{\lambda}{4 n_j}(2M+1)\left(1 - \frac{n_c^2}{n_j^2} + \frac{\lambda^2}{4 n_j^2 d_c^2}\right)^{-1/2} \tag{2}$$

.

The actual fabrication of these ARROW devices is beyond the scope of this thesis, but to give

issues that will come up further on in the paper some background; I will quickly address the

production process in which these devices are made. An illustration of this process is shown in

Figure 1-11.
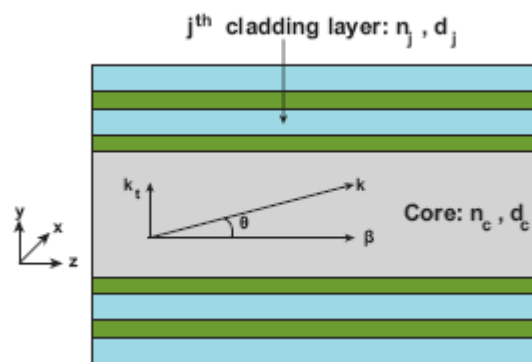
Figure 1-10 ARROW waveguide dielectric layer diagram

First alternating silicon dioxide and silicon nitride layers are deposited onto a silicon

substrate using PECVD (Plasma Enhanced Chemical Vapor Deposition) machines. Next a layer

of SU-8, a robust type of photoresist, is deposited on top of the base layers. The SU-8 is then

patterned using photolithography techniques leaving a sacrificial core that will later become the

core of the waveguide. The top layers of silicon dioxide and silicon nitride are then deposited on

top of the core. To complete this process, the sacrificial core is etched away with acid. This

leaves a hollow core surrounded by dielectric mirrors. This hollow core can be filled with gas or liquid, and light will guide within it.
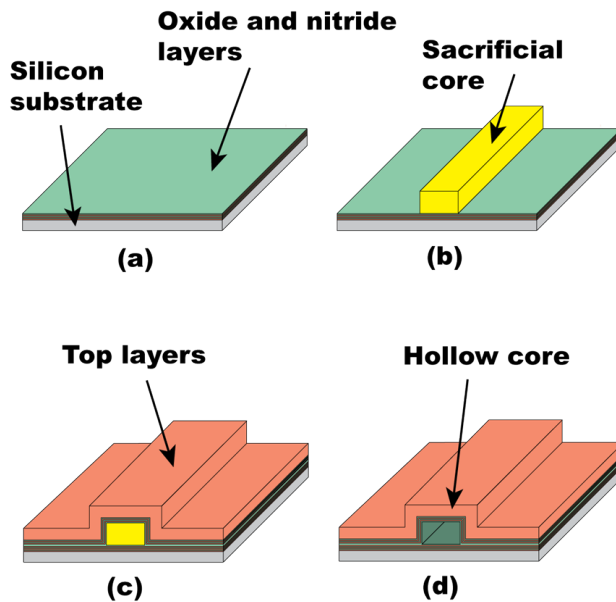
Figure 1-11 ARROW production procedure

The ARROWs are done in a specific pattern that has been developed for use in multiple projects. As different groups make improvements these improvements can be implemented in all devices made. The current schematic is shown in Figure 1-12.

The hollow and solid waveguides are clearly labeled. The chip is designed so that an optical fiber can be end coupled into the solid waveguide. The light is then guided through the solid waveguide into the hollow waveguide and back into a solid waveguide. The light can then

be detected so that any interactions that occurred within the hollow waveguide can be analyzed. There are also solid waveguides running perpendicular to the hollow waveguide that are not used in the scope of the EIT/slow light experiments. However, they are important for other groups and thus included in the ARROW schematic.
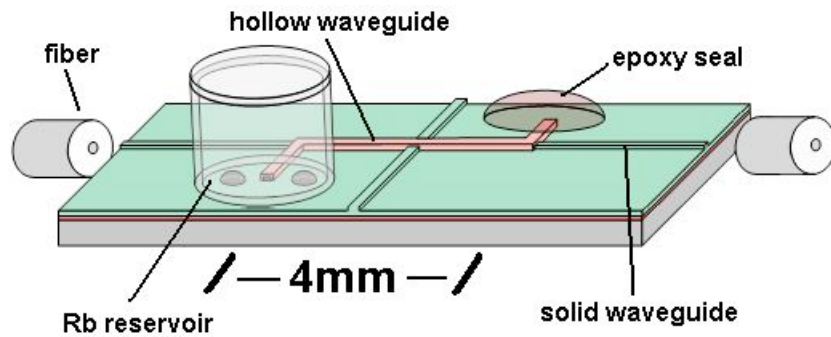
Figure 1-12 Finished ARROW device

In Figure 1-12, the rubidium reservoir is labeled. The reservoir is made out of copper and is sealed to the silicon chip by one of the sealing methods that will be detailed later in this thesis. The other end of the rubidium reservoir is sealed with a cold weld sealer.

2. Quantum Mechanical Underpinnings of EIT

EIT is a quantum optical phenomenon that causes an otherwise absorbing electrical transition to stop absorbing and thus it looks completely transparent to the incoming photons. The phenomenon seems so counterintuitive, but the math predicts this outcome, and it has been experimentally proven both by us and by other research groups. In this section, I will derive the EIT phenomenon using quantum mechanics.

2.1. Hamiltonian

Basic quantum mechanics introduces the analysis device known as the Hamiltonian. Classically, the Hamiltonian denotes the total energy in a system, comprising both kinetic and potential energy:

$$H(x,p) = \frac{p^2}{2m} + V(x)$$

(3)

However in quantum mechanics, the Hamiltonian operator is found by using the substitution $p \rightarrow \frac{\hbar}{i}\frac{\partial}{\partial x}$ to get

$$\hat{H} = -\frac{\hbar^2}{2m}\frac{\partial^2}{\partial x^2} + V(x)$$

(4)

When this is compared to the time independent Schrödinger equation

$$-\frac{\hbar^2}{2m}\frac{d^2\psi}{dx^2} + V\psi = E\psi$$

(5)

,

it is clear that the time independent Schrödinger equation can be simplified to the following

$$\hat{H}\psi = E\psi$$

(6)

.

From this simple-looking equation we can analyze the eigenstates of any quantum mechanical system and thus find the possible energies of that system. These eigenstates are orthogonal and for a simple two state system can be shown in the matrix-based analysis to be

$$\hat{H} = \begin{bmatrix} \hbar\omega_1 & 0 \\ 0 & \hbar\omega_2 \end{bmatrix} \Rightarrow \begin{bmatrix} \hbar\omega_1 & 0 \\ 0 & \hbar\omega_2 \end{bmatrix}\psi = \begin{bmatrix} E_1 & 0 \\ 0 & E_2 \end{bmatrix}\psi$$

(7)

.

2.2. Interaction of an atom with a field
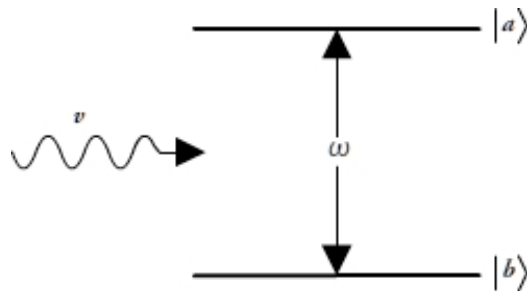
Figure 2-1 two level atom with a single mode field

18

The bare essence of EIT is how an atom reacts in an electromagnetic field. In order to understand that more fully, let's start out with the simplest possible case: a simple two-level atom and a single mode field [40]. This case is illustrated in Figure 2-1.

Let's start with the basic wave function for a two level atom. $|a\rangle$ and $|b\rangle$ represent the two upper and lower states of the atom respectively, as given by

$$|\psi(t)\rangle = C_a(t)|a\rangle + C_b(t)|b\rangle$$ (8)

where C_a and C_b are the probability amplitudes of finding the atom in the corresponding states. If we put this into the Schrödinger equation, we get:

$$|\dot{\psi}(t)\rangle = -\frac{i}{\hbar} H |\psi(t)\rangle$$ (9)

where

(10)

$$H = H_0 + H_1 .$$

In this case, similar to other cases that we'll see later on, the Hamiltonian is composed of two parts. H_0 is the unperturbed Hamiltonian of the atom, while H_1 is the perturbation that comes from the applied field.

If we use the completeness relation that states

$$\sum_n |n\rangle\langle n| = 1 \tag{11}$$

the unperturbed Hamiltonian H_0 for the two state system can be written as

$$H_0 = (|a\rangle\langle a| + |b\rangle\langle b|)H_0(|a\rangle\langle a| + |b\rangle\langle b|) = \hbar\omega_a|a\rangle\langle a| + \hbar\omega_b|b\rangle\langle b| \tag{12}$$

and

$$\left(H_o|a\rangle = \hbar\omega_a|a\rangle, H_o|b\rangle = \hbar\omega_b|b\rangle\right) \tag{13}$$

Building on this simple case, we now examine the perturbation Hamiltonian. For this case, we'll use the simplest possible perturbation: a linearly polarized field along the x-axis, as given by

$$H_1 = -exE(t) = -e(|a\rangle\langle a| + |b\rangle\langle b|)x(|a\rangle\langle a| + |b\rangle\langle b|)E(z,t) \tag{14}$$

When we substitute $\wp_{ab} = \wp_{ba}^* = e\langle a|x|b\rangle$ for the matrix element of the dipole moment, and because the expectation value $\langle a|x|a\rangle$ in a linearly polarized field is zero, we get

20

$$H_1 = -(\wp_{ab}|a\rangle\langle b| + \wp_{ba}|b\rangle\langle a|)E(t) \qquad (15)$$

Next we make the following substitutions and approximations,

$$\wp_{ba} = |\wp_{ba}|e^{i\phi} \text{ (}\phi \text{ is the phase of the dipole matrix element)}$$

$$E(t) = E\cos(vt)\text{(v=ck is the frequency of the field)} \qquad (16)$$

$$= \frac{E}{2}(e^{ivt} + e^{-ivt})$$

We also define the Rabi frequency Ω_R here in terms of the dipole matrix element just introduced, so

$$\Omega_R = \frac{|\wp_{ba}|E}{\hbar} \qquad (17)$$

All of these are then put together into the Hamiltonian and we solve the Schrödinger equation for this system under this perturbation. There is much more complicated math involved in this calculation, but for now, the perturbed Hamiltonian will be sufficient. The perturbed Hamiltonian will be written as

$$H_1 = -\frac{\hbar}{2}\Omega_R(e^{i\phi}(e^{ivt} + e^{-ivt})|a\rangle\langle b| + e^{-i\phi}(e^{ivt} + e^{-ivt})|b\rangle\langle a|) \qquad (18)$$

This is complicated, but it illustrates the process of finding the perturbations due to applied fields and also illustrates the necessity to find simpler ways to express these complex interactions between fields and atoms.

2.3. Coherent Trapping – Dark States

Coherent population trapping is a phenomenon in which atoms are driven into one particular quantum state that and there are no possible transitions out of that particular state. In other words, the atoms become trapped in that state.

We just solved the Hamiltonian for the simplest possible situation. But this is not the interesting aspect of this problem, in order to see the real possibilities, we must solve for a more complicated situation. We will start with the lambda energy structure that will be discussed further at a later point in this thesis. The Lambda structure has two dipole allowed transitions and one dipole forbidden transmissions.

As calculated earlier, we would like to find the unperturbed Hamiltonian and the perturbation Hamiltonian in order to form the entire Hamiltonian, so a quick reminder that

$$H = H_0 + H_1 \ .$$

(19)

The Hamiltonian for the new system can be found by generalizing the Hamiltonian found in the simple system earlier in this analysis to form

$$H_0 = \hbar\omega_a |a\rangle\langle a| + \hbar\omega_b |b\rangle\langle b| + \hbar\omega_c |c\rangle\langle c|$$

(20)

and

$$H_1 = -\frac{\hbar}{2}(\Omega_{R1} e^{-i\phi_1} e^{-i\nu_1 t} |a\rangle\langle b| + \Omega_{R2} e^{-i\phi_2} e^{-i\nu_2 t} |a\rangle\langle c|) + H.c.$$

(21)

In this case, H.C. signifies the Hermitian Conjugate of the previous part of the equation. The Hamiltonian only addresses the transitions between $|a\rangle$ and $|b\rangle$, and $|a\rangle$ and $|c\rangle$ as these are the allowed dipole transitions.

The atomic wave function of the entire system will be written with a probability amplitude and complex phase for each of the original energy states, so that

$$|\psi(t)\rangle = c_a(t)e^{-i\omega_a t}|a\rangle + c_b(t)e^{-i\omega_b t}|b\rangle + c_c(t)e^{-i\omega_c t}|c\rangle \qquad (22)$$

.

When this wave function is placed in the Schrödinger with Hamiltonian that was described earlier in this section, three equations of motion can be derived:

$$\dot{c}_a = \frac{i}{2}(\Omega_{R1}e^{-i\phi_1}c_b + \Omega_{R2}e^{-i\phi_2}c_c)$$

,

$$\dot{c}_b = \frac{i}{2}\Omega_{R1}e^{-i\phi_1}c_a$$

, $\qquad (23)$

and

$$\dot{c}_c = \frac{i}{2}\Omega_{R2}e^{-i\phi_2}c_a$$

.

These three equations are calculated under the assumption that the fields are resonant with the transitions of

$|a\rangle$ and $|b\rangle$, and $|a\rangle$ and $|c\rangle$, i.e. $\omega_{ab} = v_1$ and $\omega_{ac} = v_2$.

As always, in order to solve these kinds of differential equations we need to have the initial conditions. So we're going to assume that the initial atomic state is a superposition of the two lower levels as shown by

$$|\psi(0)\rangle = \cos(\theta/2)|b\rangle + \sin(\theta/2)|c\rangle \qquad (24)$$

.

With the equations of motion that were calculated from the Schrödinger equation and the initial conditions, it's possible to solve for the probability amplitudes

$$c_a(t) = \frac{i\sin(\Omega t/2)}{\Omega}\left[\Omega_{R1}e^{-i\phi_1}\cos(\theta/2) + \Omega_{R2}e^{-i(\phi_2+\psi)}\sin(\theta/2)\right]$$

,

$$c_b(t) = \frac{1}{\Omega^2}\{[\Omega_{R2}^2 + \Omega_{R1}^2\cos(\Omega t/2)]\cos(\theta/2) - 2\Omega_{R1}\Omega_{R2}e^{i(\phi_1-\phi_2-\psi)}\sin^2(\Omega t/4)\sin(\theta/2)\}$$

,

and

$$c_c(t) = \frac{1}{\Omega^2}\{-2\Omega_{R1}\Omega_{R2}e^{-i(\phi_1-\phi_2)}\sin^2(\Omega t/4)\cos(\theta/2) + [\Omega_{R1}^2 + \Omega_{R2}^2\cos(\Omega t/2)]e^{-i\psi}\sin(\theta/2)\}$$

(25)

where

$$\Omega = \left(\Omega_{R1}^2 + \Omega_{R2}^2\right)^{1/2}$$

.

With these conditions in place, it is possible to calculate where coherent population trapping occurs. When the

$$\Omega_{R1} = \Omega_{R2} \quad ,$$

$$\theta = \pi / 2 \quad , \tag{26}$$

and

$$\phi_1 - \phi_2 - \psi = \pm \pi$$

are met, the probability amplitudes can be calculated as shown by

$$c_a(t) = 0 \quad ,$$

$$c_b(t) = \frac{1}{\sqrt{2}} \quad ,$$

$$\tag{27}$$

and

$$c_c(t) = \frac{1}{\sqrt{2}} e^{-i\psi} \quad .$$

The result is that when the appropriate resonant fields are applied, there is no possibility for the system to be found in the $|a\rangle$ state. Or there is no absorption of the field to transition out of the two lower states. This is called population trapping.

The Hamiltonian for EIT can be generated from the previously calculated Hamiltonian with a few substitutions, namely

$$\Omega_{R1} e^{-i\phi_1} e^{-i\nu_1 t} = \frac{\wp_{ab} E}{\hbar} e^{-i\nu t}$$

and

$$\Omega_{R2} e^{-i\phi_2} e^{i\nu_2 t} = \Omega_c e^{-i\phi_c} e^{-\nu_c t} \quad .$$

(28)

This will result in the interaction Hamiltonian for the atom and the two fields that will be used in explaining EIT of

$$H = H_0 + H_1 \quad ,$$

where

$$H_0 = \hbar\omega_a |a\rangle\langle a| + \hbar\omega_b |b\rangle\langle b| + \hbar\omega_c |c\rangle\langle c|$$

(29)

and

$$H_1 = -\frac{\hbar}{2}(\frac{\wp_{ab} E}{\hbar} e^{-i\nu t} |a\rangle\langle b| + \Omega_c e^{-i\phi_c} e^{-\nu_c t} |a\rangle\langle c|) + H.c. \quad .$$

2.4. Energy Scheme Requirements

In order for EIT or Coherent Population Trapping to occur, the atoms in the interaction substance must have a particular energy scheme. Although there are likely to be many more energy states available in the atoms, we must be able to simplify them down to three energy states. By applying coherent beams of light (laser beams) at specifically tuned frequencies, we are able to treat a complicated set of energies as a simple three energy state system.

However, a simple three state system is not enough. The system must follow specific dipole selection rules. Of the three transitions available, two of them must be dipole allowed – the transitions can be induced by an oscillating electric field, which would include a laser beam. The third transition must be dipole forbidden. Quantum mechanically, this transition is very unlikely to happen, and as such we can classify it as forbidden. The dipole allowed transitions correspond with the applied laser fields.

Figure 2-2 shows the possible ways that these energy transitions can be found. In a *Ladder* (also called *Cascade*) scheme $|3\rangle > |2\rangle > |1\rangle$ and the forbidden transition is between $|1\rangle$ and $|3\rangle$. In a *Lambda* scheme $|2\rangle > |1\rangle$ and $|3\rangle$. However, in a symmetric *Lambda* scheme, $|1\rangle$ and $|3\rangle$ are degenerate or close to degenerate. In a *Vee* scheme $|1\rangle < |2\rangle$ and $|3\rangle$. Similar to a *Vee* scheme, a symmetric *Vee* scheme has $|2\rangle$ and $|3\rangle$ almost degenerate. In all of these schema, $|3\rangle$ is a metastable state. The electrons that end up in it will stay there for a relatively long time in comparison to other non-metastable states – they will have a long lifetime.

Coherent Population Trapping can occur in any of these schemes. However, EIT is associated with only *Lambda* schema, because EIT does not require a population transfer, while

as the name suggests, Coherent Population Trapping involves movement of populations. EIT also requires the presence of a metastable dark state and Coherent Population Trapping does not.
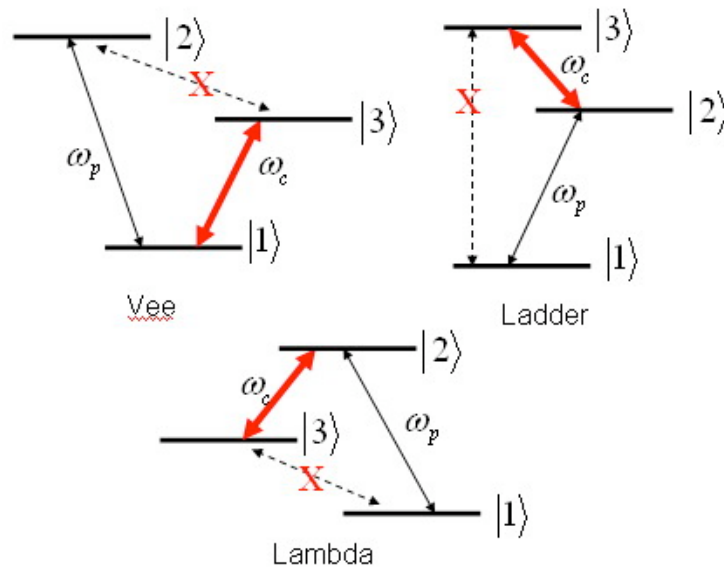
Figure 2-2 The three possible schema for the energy states involved in CPT and EIT. In each of these schema, two of the transitions are dipole allowed, while the third one is a forbidden transition

2.5. Rabi Frequency

In quantum mechanical derivations, we often use a substitution called the Rabi Frequency to illustrate the strength of the coupling between the applied electromagnetic field and the dipole transition. In the case of resonance to the transition, Rabi Flopping will occur at the same transition as the Rabi frequency. This is a measure of the cyclic absorbing and re-emitting of photons of a given dipole allowed transition. The Rabi Frequency is

$$\chi_{ij} = \frac{\vec{d}_{ij} \cdot \vec{E}_0}{\hbar}$$ (30)

.

$\vec{E}_0$ refers to the applied Electric field, while $\vec{d}_{ij}$ refers to the dipole transition moment for the $i \rightarrow j$ transition. In calculating the dipole transition moment, an integral is taken over 3-dimensional space of the product of the wave functions of the initial and final states of the transition with the dipole moment operator.

The dipole moment operator is

$$\hat{d} = e(\sum_i x_i, \sum_j y_j, \sum_k z_k)$$, (31)

where the summations are over the positions of the electrons in the system. Using this dipole moment operator, we are able to calculate the dipole transition moment as given by

$$d_{nm} = \int \Psi_n^* \hat{d} \Psi_m d^3 r = \langle \Psi_n | \hat{d} | \Psi_m \rangle$$ (32)

.

Importantly, the dipole transition moment will tell us whether a transition is dipole allowed or forbidden. In general, if we are transitioning between an even and an odd wave function, the integral will be nonzero and thus, the transition is allowed. If the transition is between an even and an even wave function or an odd and an odd transition, the integral will be zero, thus signifying a forbidden transition.

Often we don't use the Rabi frequency itself, but instead we use the generalized Rabi frequency, which factors in the detuning away from the transition resonance. The generalized frequency is

$$\Omega_{ij} = \sqrt{\left|\chi_{ij}\right|^2 + \Delta^2}$$

Δ refers to the detuning, or the difference between the applied frequency and the frequency associated with the transition ($\Delta = \omega_{light} - \omega_{transition}$).

The Rabi frequency will be used in the derivation for both EIT and CPT. It is a measurement of the coupling strength between the electric field and the dipole transition moment. With it, we will be able to determine the "ease" of the transition occurring.

2.6. Dressed State Analysis

In the "dressed states" derivation of EIT, the bare atom Hamiltonian H_0 is modified to include the interactions with the electric fields provided by the coupling beam and the probe beam H_1. Remember that

$$H = H_0 + H_1$$

When this new Hamiltonian is analyzed, we will better be able to understand the system and the EIT result will be clear.

In this particular derivation [11] it is helpful to start by considering CPT (Coherent Population Trapping). EIT is a subset of CPT, therefore at least partial understanding of CPT will be important in understanding EIT. Both CPT and EIT involve laser fields interacting with

energy states within the atoms, when in turn creates coherent superposition of the atomic basis states.
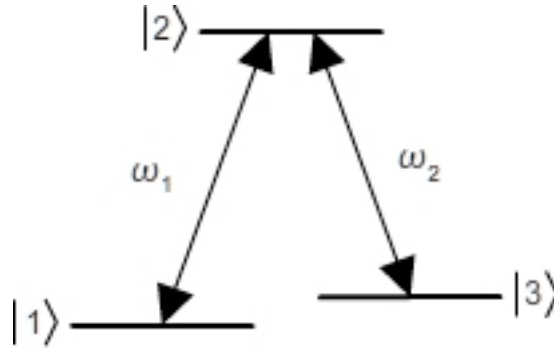
Figure 2-3 Lambda scheme for EIT and CPT

First the Λ 3-state scheme that is shown in Figure 2-3 will be discussed. The near-resonant fields that couple the states together are defined in terms of their Rabi frequencies with strengths of Ω_1 (at frequency ω_1) and Ω_2 (at frequency ω_2). Further definitions are:

the frequency of transitions between states are $\omega_{12} = \dfrac{E_1 - E_2}{\hbar}$ and

$$\omega_{23} = \frac{E_2 - E_3}{\hbar}$$

, (35)

the one photon frequency detunings are $\Delta_{12} = \omega_{12} - \omega_1$ and

$$\Delta_{23} = \omega_{23} - \omega_2$$

,

31

the two photon (Raman) frequency detuning is

$$\delta = (\omega_{12} - \omega_{23}) - (\omega_1 - \omega_2)$$

,

and finally the Rabi Frequency is

$$\Omega_i = \mu_i \cdot E_0$$

.

where E_0 is the amplitude of the electric field and μ_i is the transition electronic dipole moment.

The addition of the laser fields modifies the bare atom Hamiltonian H0 with the interaction $V_j = \hbar\Omega_j$ from the laser field coupling. Resulting in a Hamiltonian of

$$H = H_0 + V_1 + V_2 \tag{36}$$

.

However, the resulting Hamiltonian is complicated and not at all easy to use. At this point the rotating wave approximation (RWA) steps in to make the analysis a little easier and simpler to understand. The RWA is often used in atomic optics. In this approximation terms within the Hamiltonian with rapid oscillations are neglected. This is only valid at low electric field intensities and when the applied electric field is at or near resonance for a given atomic energy transition. The resulting Hamiltonian after the rotating wave approximation is

$$H = -\frac{\hbar}{2}\begin{bmatrix} 0 & 0 & \Omega_p \\ 0 & -2(\Delta_1 - \Delta_2) & \Omega_c \\ \Omega_p & \Omega_c & -2\Delta_1 \end{bmatrix} \tag{37}$$

.

The eigenstates of this new Hamiltonian can be complicated but can be simplified by expressing them in terms of the mixing angles θ and φ, which are each related to the Rabi frequency (Ω) and the one and two photon detunings. At two-photon resonance ($\Delta_1 = \Delta_2$ or $\delta = 0$) the mixing angles are:

$$\tan\theta = \frac{\Omega_p}{\Omega_c}$$

and

$$\tan 2\phi = \frac{\sqrt{\Omega_p^2 + \Omega_c^2}}{\Delta}$$

.

(38)

With these substitutions, the eigenstates in terms of the bare atomic states that we started out with are simply

$$\left|a^+\right\rangle = \sin\theta\sin\phi\left|1\right\rangle + \cos\phi\left|3\right\rangle + \cos\theta\sin\phi\left|2\right\rangle$$

,

$$\left|a^0\right\rangle = \cos\theta\left|1\right\rangle - \sin\theta\left|2\right\rangle$$

,

(39)

and

$$\left|a^-\right\rangle = \sin\theta\cos\phi\left|1\right\rangle - \sin\phi\left|3\right\rangle + \cos\theta\cos\phi\left|2\right\rangle$$

.

Of particular note is the fact that $\left|a^0\right\rangle$ has no element of state $\left|3\right\rangle$ in it. As a result, once an electron is in state $\left|a^0\right\rangle$, there is no possibility of excitation and consequent spontaneous

33

emission in which would end up in a different state. Therefore, $\left|a^0\right\rangle$ is referred to as the dark state. This is the basic principle behind coherent population trapping, because much of the population will end up trapped in this state.

Another way to express these eigenstates without the mixing angles is here [12]: The eigenstates resulting from this new Hamiltonian will be linear superpositions of the original three bare atomic states. However, at exactly two photon resonance when the detuning is reduced to zero ($\Delta=0$), two of those Hamiltonian eigenstates are symmetric and antisymmetric coherent superpositions of the lower energy states $\left|1\right\rangle$ and $\left|3\right\rangle$. The two eigenstates are the

$$\text{symmetric eigenstate is } \frac{\Omega_1}{\Omega'}\left|1\right\rangle + \frac{\Omega_2}{\Omega'}\left|3\right\rangle$$

$$\text{and the antisymmetric eigenstate is } \frac{\Omega_1}{\Omega'}\left|1\right\rangle - \frac{\Omega_2}{\Omega'}\left|3\right\rangle \text{ ,} \tag{40}$$

$$\text{where } \Omega' = \sqrt{\Omega_1^2 + \Omega_2^2}$$

and Ω' acts to normalize the two eigenstates.

When looking at these two eigenstates it is important to note that the bare state $\left|2\right\rangle$ does not factor into either of these superpositions. The symmetric eigenstate will be referred to as $\left|+\right\rangle$ and likewise, the antisymmetric eigenstate will be referred to as $\left|-\right\rangle$. As we further study these two eigenstates, it becomes clear that if Ω_1 and Ω_2 are balanced appropriately the negative sign will ensure that the total amplitude of the eigenstate will be zero.

34

So, as we've discussed, we are able to achieve CPT through getting electrons into a state that they can't be excited out of and then the population will be "trapped" in that state. But now I want to extend this concept to EIT and to use this same notation to explain it. In CPT, the two laser beams are roughly of the same energy. However, in EIT, the coupling beam (between $|2\rangle$ and $|3\rangle$) has a much higher intensity than the probe beam (between $|1\rangle$ and $|3\rangle$). Consequently $\Omega_p << \Omega_c$, and therefore $\sin\theta \rightarrow 0$ and $\cos\theta \rightarrow 1$. When these assumptions are made, the eigenstates become

$$|a^+\rangle = \cos\phi|3\rangle + \sin\phi|2\rangle$$,

$$|a^0\rangle = |1\rangle$$, (41)

and

$$|a^-\rangle = \cos\phi|2\rangle - \sin\phi|3\rangle$$.

Further simplification comes through assuming the probe is on resonance so Δ=0. If that is the case, $\tan\phi \rightarrow 1$ and ϕ=π/2. The eigenstates then become

$$|a^+\rangle = \frac{1}{\sqrt{2}}\left(|3\rangle + |2\rangle\right)$$, (42)

35

$$\left|a^0\right\rangle = \left|1\right\rangle$$
,

and

$$\left|a^-\right\rangle = \frac{1}{\sqrt{2}}\left(\left|2\right\rangle - \left|3\right\rangle\right)$$
.

If we want to see them in an energy diagram, these eigenstates will look like what is shown in Figure 2-4:
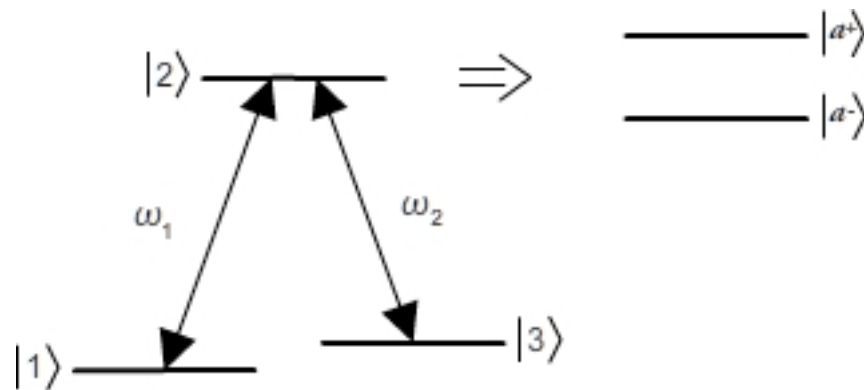
Figure 2-4 Splitting of energy states because of EIT

From the energy diagram shown in figure 2-4, it's clear to see that any beam that is tuned to the $\left|1\right\rangle \to \left|3\right\rangle$ transition would not be absorbed because there are no empty states at those energy levels. But a photon with slightly more energy than the transition or slightly less energy than the transition would cause an electron to be energized and jump up to the higher energy level. This is the essence of EIT. An energy transition that with no applied fields would absorb

incoming photons now stops absorbing those photons and thus looks transparent. This is shown

in Figure 2-5.
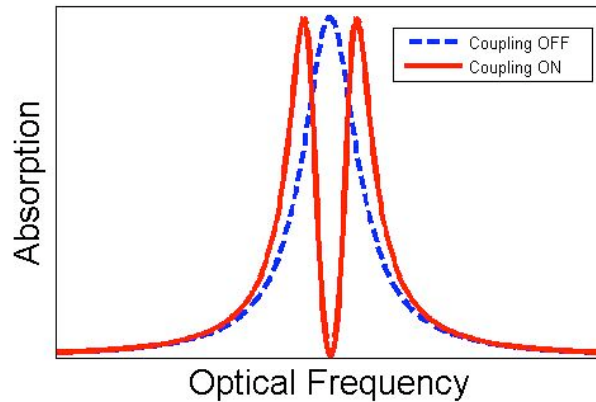
Figure 2-5 This figure shows the absorption of the EIT substance as a function of the incoming laser beam frequency. The blue dashed line shows the absorption profile of a given electronic transition with the coupling beam turned off. Turning the coupling beam on however causes that same transition to become transparent as shown by the red solid line. This is the essence of EIT

2.7. Density Matrix Derivation of EIT

Thus far the essence of EIT has been derived using unperturbed and perturbed Hamiltonians and the Schrödinger. From there, the eigenstates and eigenvalues of the system were calculated, thus revealing the basic principles behind EIT and showing how an initially opaque transition becomes transparent.

The quantum Density Operator provides another way to derive the EIT that gives further insight into the quantum workings behind this slightly mysterious phenomenon. The Density Operator is often represented in matrix form and is called the Density Matrix. For this reason,

when looking for information about the density operator or the density matrix, it's important to not neglect the other.

The Density Operator is used to describe a mixed system, or a system with a collection of possible states. It includes the statistical probability of the system being in one of those states. A system where the state is perfectly known is called a pure state. In a pure state, there is the possibility of quantum interference due to the coherence in the state. A mixed state, on the other hand, is composed of a classical statistical mixture of pure states that each occurs at a different probability. There is no interference within a mixed state due to the lack of coherence

The Density Operator is defined as

$$\rho = \sum_{i=1}^{n} p_i |\psi_i\rangle\langle\psi_i|$$

(43)

where p_i is the probability of that particular state occurring [6].

When the Density Operator is represented as a matrix, the off-diagonal element will represent how much interference will occur between states. A pure state will exhibit non-zero off-diagonal elements, while a mixed state's diagonal elements will be zero.

First, it will be helpful for us to derive the density matrix equation of motion. In order to do this, we start with the Schrödinger equation, which is

$$|\dot{\psi}\rangle = -\frac{i}{\hbar} H |\psi\rangle$$

(44)

.

When the time-derivative is taken of ρ, we get

$$\dot{\rho} = \sum_i^n p_i \left(|\dot{\psi}_i\rangle\langle\psi_i| + |\psi_i\rangle\langle\dot{\psi}_i| \right)$$

(45)

If we use the Schrödinger equation to replace $|\psi\rangle$ and $|\dot{\psi}\rangle$ we get an equation that is known as the Liouville or Von Neumann equation of motion for the density matrix. The equation is written as

$$\dot{\rho} = -\frac{i}{\hbar}[H,\rho]$$

(46)

where $[H,\rho]$ is the commutator between H and ρ. The commutator of $[x,y]$ is xy-yx.

This equation is useful because it can give us statistical information about the system in addition to the quantum mechanical information that we would get from Schrödinger equation alone. This is because the density operator contains that statistical information.

However, this equation is missing a critical element. In order for it to be more accurate we need to factor in decays from excited states due to spontaneous emission. This decay can be integrated by using the relaxation matrix Γ. This is defined by

$$\langle n|\Gamma|m\rangle = \gamma_n \delta_{nm}$$

(47)

By adding this new term, the new density matrix equation of motion becomes

$$\dot{\rho} = -\frac{i}{\hbar}[H,\rho] - \frac{1}{2}\{\Gamma,\rho\}$$

(48)

,

where $\{\Gamma,\rho\} = \Gamma\rho + \rho\Gamma$. With this new and improved density matrix equation of motion, we can explicitly define the elements of the matrix. The ijth element of the matrix just defined can be written as

$$\dot{\rho}_{ij} = -\frac{i}{\hbar}\sum_k (H_{ik}\rho_{kj} - \rho_{ik}H_{kj}) - \frac{1}{2}\sum_k (\Gamma_{ik}\rho_{kj} + \rho_{ik}\Gamma_{kj})$$

(49)

.

With this defined, we're in business for EIT. But first, a few more definitions: Levels $|a\rangle$ and $|b\rangle$ are coupled by a probe field with amplitude E and frequency ν. Levels $|a\rangle$ and $|c\rangle$ are coupled by a strong coherent coupling field of frequency ν_c with a complex Rabi frequency $\Omega_c e^{-i\phi_c}$. And the off diagonal elements of the relaxation matrix for ρ_{ab}, ρ_{ac}, and ρ_{cb} are γ_1, γ_2, and γ_3 respectively. Given these known variables, we can calculate the matrix elements in the density matrix elements. These become

$$\dot{\rho}_{ab} = -(i\omega_{ab} + \gamma_1)\rho_{ab} - \frac{i}{2}\frac{\wp_{ab}E}{\hbar}e^{-i\nu t}(\rho_{aa} - \rho_{bb}) + \frac{i}{2}\Omega_c e^{-i\phi_c}e^{-i\nu_c t}\rho_{cb}$$

,

$$\dot{\rho}_{cb} = -(i\omega_{cb} + \gamma_3)\rho_{cb} - \frac{i}{2}\frac{\wp_{ab}E}{\hbar}e^{-i\nu t}\rho_{ca} + \frac{i}{2}\Omega_c e^{-i\phi_c}e^{-i\nu_c t}\rho_{ab}$$

,

and

$$\dot{\rho}_{ac} = -(i\omega_{ac} + \gamma_2)\rho_{ac} - i\Omega_c e^{i\phi_c} e^{-i\nu_c t}(\rho_{aa} - \rho_{cc}) + \frac{i}{2}\frac{\wp_{ab}E}{\hbar}e^{-i\nu t}\rho_{bc} \qquad (50)$$

.

EIT is caused by a very strong coupling field, which is represented by the value Ω_c. For this reason, the terms which are involved with Ω_c cannot be simplified. We must keep it whole and include all of its orders.

Like any differential equation, we must have some initial conditions to solve the equations completely. The atoms start out initially in the ground state, so it is possible to say that

$$\rho_{bb}^{(0)} = 1 \quad ,$$

and (51)

$$\rho_{aa}^{(0)} = \rho_{cc}^{(0)} = \rho_{ca}^{(0)} = 0 \quad .$$

The following substitutions can also be made:

$$\rho_{ab} = \tilde{\rho}_{ab}e^{-i\nu t} \quad ,$$

and (52)

$$\rho_{cb} = \tilde{\rho}_{cb}e^{-i(\nu + \omega_{ca})t} \quad .$$

When all of these assumptions are made, this coupled set of equations is obtained:

$$\dot{\tilde{\rho}}_{ab} = -(\gamma_1 + i\Delta)\tilde{\rho}_{ab} + \frac{i}{2}\frac{\wp_{ab}E}{\hbar} + \frac{i}{2}\Omega_c e^{-i\phi_c}\tilde{\rho}_{cb}$$

,

and   (53)

$$\dot{\tilde{\rho}}_{cb} = -(\gamma_3 + i\Delta)\tilde{\rho}_{cb} + \frac{i}{2}\Omega_c e^{-i\phi_c}\tilde{\rho}_{ab}$$

.

In these equations, $\Delta = \omega_{ab} - \nu$ is the detuning of the probe field, and we have made the

substitution $\nu_c = \omega_{ac}$.

Using some matrix algebra these two equations can be solved. First, we write them in

matrix form like this:

$$\dot{R} = -MR + A$$,   (54)

with

$$R = \begin{bmatrix} \tilde{\rho}_{ab} \\ \tilde{\rho}_{cb} \end{bmatrix}$$

,

$$M = \begin{bmatrix} \gamma_1 + i\Delta & -\frac{i}{2}\Omega_c e^{-i\phi_c} \\ -\frac{i}{2}\Omega_c e^{i\phi_c} & \gamma_3 + i\Delta \end{bmatrix}$$

,

and

42

$$A = \begin{bmatrix} i\wp_{ab}E/2\hbar \\ 0 \end{bmatrix} . \tag{55}$$

Integrating the above equations yields

$$R(t) = \int_{-\infty}^{t} e^{-M(t-t')} A \, dt' \tag{56}$$

$$= M^{-1}A , $$

with a final result of

$$\rho_{ab}(t) = \frac{i\wp_{ab}Ee^{-ivt}(\gamma_3 + i\Delta)}{2\hbar\left[(\gamma_1 + i\Delta)(\gamma_3 + i\Delta) + \Omega_c^2/4\right]} . \tag{57}$$

Next, it's possible to relate the density matrix elements to the complex polarization using the definition of the complex polarization, which is

$$P(z,t) = 2\wp \, \rho_{ab} e^{i[vt - kz + \phi(z,t)]} \tag{58}$$

as well as the relation between the complex polarization, applied Electric field and the complex susceptibility, which is defined as

$$P = \varepsilon_o \chi E . \tag{59}$$

When equations (58) and (59) are used along with the equation we have already derived for the density matrix elements (50), it is possible to write out the real and imaginary parts of the complex susceptibility as

$$\chi = \chi' + i\chi'' \quad ,$$

where

$$\chi' = \frac{N_a|\wp_{ab}|^2\Delta}{\varepsilon_o\hbar Z}\left[\gamma_3(\gamma_1 + \gamma_3) + \left(\Delta^2 - \gamma_1\gamma_3 - \frac{\Omega_c^2}{4}\right)\right] \quad , \tag{60}$$

and

$$\chi'' = \frac{N_a|\wp_{ab}|^2}{\varepsilon_o\hbar Z}\left[\Delta^2(\gamma_1 + \gamma_3) - \gamma_3\left(\Delta^2 - \gamma_1\gamma_3 - \frac{\Omega_c^2}{4}\right)\right] \quad .$$

In these equations, N_a is the atomic number density, while Z is

$$Z = \left(\Delta^2 - \gamma_1\gamma_3 - \frac{\Omega_c^2}{4}\right)^2 + \Delta^2(\gamma_1 + \gamma_3)^2 \quad . \tag{61}$$

When the real and imaginary parts of the complex susceptibility are plotted vs. the detuning, we get the plot shown in Figure 2-6 [40].

The real and imaginary parts of the complex susceptibility are directly related to the index of refraction and the absorption of the guiding material. Let's go look into that further.

It was previously stated that

$$P = \varepsilon_o\chi E \tag{62}$$

.

44

Since the susceptibility is complex and has both a real and imaginary part, we can extrapolate to get the real,

$$\mathrm{Re}\, P = \varepsilon_o E \chi' \quad,$$

and imaginary,

(63)

$$\mathrm{Im}\, P = \varepsilon_o E \chi'' \quad,$$

parts of the complex polarization.
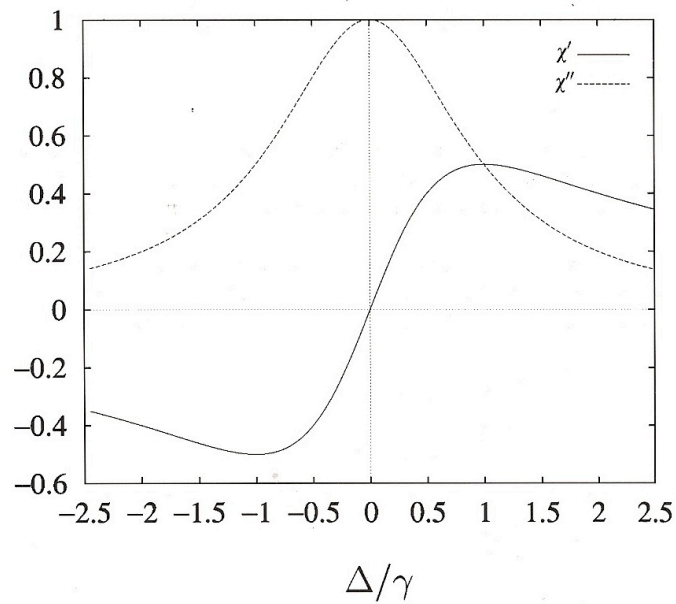
Figure 2-6 Real and imaginary parts of the linear susceptibility as a function of the detuning

These can be utilized in

$$\frac{\partial E}{\partial z} + \frac{1}{c}\frac{\partial E}{\partial t} = -\kappa E - \frac{1}{2\varepsilon_o}k\operatorname{Im}P$$

and   (64)

$$\frac{\partial \phi}{\partial z} + \frac{1}{c}\frac{\partial \phi}{\partial t} = k - \frac{v}{c} - \frac{1}{2\varepsilon_o}\frac{k}{E}\operatorname{Re}P$$

to make some important intuitive jumps. From these equations, we can see that the imaginary part of the susceptibility represents the loss per unit wavelength, while the real part of the susceptibility represents the dispersion per unit wavelength.

But really, in order to get these in even more understandable terms, it's necessary to do even more massaging. Let's pull in the dispersion relation of

$$k^2 - \frac{v^2}{c^2}n^2 = 0$$
,

and just to clarify,   (65)

$$n^2(v) = 1 + \chi^2(v)$$
.

Once again, by expressing n as a complex number as we have before will be helpful. Thus

$$n = n' + in'' \quad , \tag{66}$$

given the parameters of

$$n' + in'' = (1 + \chi' + i\chi'')^{1/2}$$

$$= \left[(1 + \chi')^2 + \chi''\right]^{1/4} \exp\left[i\,\mathrm{sgn}(\chi'')\theta/2\right] \tag{67}$$

.

This last equation has the substitution

$$\theta = \tan^{-1}\left(\frac{|\chi''|}{1 + \chi'}\right) \tag{68}$$

.

By separating the real and imaginary parts we can solve for n' and n'' as

$$n' = \left\{\frac{\left[(1 + \chi')^2 + \chi''^2\right]^{1/2} + (1 + \chi')}{2}\right\}^{1/2} \quad ,$$

and $\tag{69}$

$$n'' = \left\{\frac{\left[(1 + \chi')^2 + \chi''^2\right]^{1/2} + (1 + \chi')}{2}\right\}^{1/2} \mathrm{sgn}(\chi'')$$

.

We have just solved for something that is much easier to understand than we've seen in the past few pages. n' is the refractive index of the guiding medium and n'' is the absorption coefficient associated with the medium.

3. Towards Slow Light

3.1. Kramer's-Kronig Relations

The Kramers-Kronig relations come into play when we talk about slow light. Just as was derived using the density matrix equations, the Kramers-Kronig relations tell us that the dispersive and absorptive properties of a medium are not independent and that if the absorption of the medium changes, the dispersion must of necessity change.

I would love to derive these equations in this thesis to help those reading know the logic and use behind them. However, they are not easy equations to derive. Suffice it to say that they are legitimate and have been successfully tested and vetted over and over, so we can use them without worry.

These equations, interestingly, originated with Ralph Kronig and Hendrik Anthony Kramers independently in 1926 and 1927 respectively. Kronig and Kramer both used them to describe the relationship between absorption and dispersion in materials. Since then, however, these relationships have been adopted by mathematicians and have been used as pure mathematical concepts. But they are still often used in the context of the relationship between absorption and dispersion of light waves.

The Kramers Kronig relations can be expressed as

$$\text{Re}\left(\frac{\varepsilon(\omega)}{\varepsilon_o}\right) = 1 + \frac{1}{\pi} P \int_{-\infty}^{\infty} \frac{\text{Im}\left(\frac{\varepsilon(\omega)}{\varepsilon_o}\right)}{\omega' - \omega} d\omega'$$

,

and (70)

$$\text{Im}\left(\frac{\varepsilon(\omega)}{\varepsilon_o}\right) = -\frac{1}{\pi} P \int_{-\infty}^{\infty} \frac{\text{Re}\left(\frac{\varepsilon(\omega)}{\varepsilon_o}\right) - 1}{\omega' - \omega} d\omega'$$

.

In these equations, P stands for the Cauchy principle value, and the ε as usual stands for the permittivity of the material.

It's clear to see that given either the imaginary or real part of the permittivity, it would be possible to calculate the other part. Previously, we were able to derive the real and imaginary terms of the complex susceptibility. Fortunately, the permittivity and the complex susceptibility are related to each other and to the index of refraction.

$$\varepsilon = \varepsilon_r \varepsilon_o = (1 + \chi)\varepsilon_o$$

and (71)

$$n = \sqrt{\varepsilon_r \mu_r}$$

directly relate the permittivity to the index of refraction and the susceptibility, where μ_r is the relative permeability of the substance.

50

Once again, to remind the reader, the real part of the index of refraction will be related to the dispersion of the electromagnetic wave in the guiding substance and the imaginary part will be related to the absorption of the same electromagnetic wave in the guiding substance.

3.2. Slow Light

When the speed of light is discussed, it's important to know exactly what speed is being addressed. Any wave packet has two velocities associated with it: the group velocity and the phase velocity. The group velocity is the velocity at which the packet itself moves. However, the speed of the phase of one frequency component of the wave packet is called the phase velocity. The group velocity and phase velocity are defined as

$$v_p = \frac{\omega}{k}$$

,

and   (72)

$$v_g = \frac{\partial \omega}{\partial k}$$

,

respectively. In both of these equations, ω refers to the angular frequency of the signal while k refers to the wavenumber.

In general, the group velocity is ultimately the more used of the two velocities because it refers to the actual velocity of the envelope of the propagating pulse. This corresponds to the speed that actual information can travel. However, in general, when the index of refraction is

51

being discussed, the velocity in that case is the phase velocity. The relationship between the phase velocity and the index of refraction is

$$v_p = \frac{c}{n}$$

,

or similarily

$$n = \frac{c}{n_p}$$

.

However, many times it's more helpful to have the index of refraction that corresponds with the group velocity. This would be defined as

$$n_g = \frac{c}{v_g}$$

.

(74)

Consequently, the group index of refraction can be written as

$$n_g = n - \omega_p \frac{dn}{d\omega_p}$$

,

(75)

where λ_o is the wavelength in vacuum. This is easy to use, since wavelengths are generally quoted for vacuum conditions.

The group velocity is then

$$v_g = \frac{c}{n - \omega_p \dfrac{dn}{d\omega_p}}$$

(76)

.

Clearly we can understand from these equations that if the index of refraction as a function of the wavelength or frequency of the light is changing quickly, the group velocity will be influenced sharply.

For this reason, if we know the relationship between the index of refraction and the wavelength, we will be able to find the actual group velocity, or the actual velocity that a given pulse will have as it travels through the guiding medium.

You can't arrive at EIT classically, but once you have EIT, you can derive slow light classically. Because, any time there is a change in the absorption, there will of necessity be a change in the dispersion, and thus a change in the group velocity.

As the index of refraction is being addressed right here, I'd like to look at what exactly the index of refraction is. Any beginning physics class will teach that the index of refraction of any given material is equal to the ratio between the speed of light in vacuum to the speed of light in that material, or

$$n = \frac{c}{v}$$

(77)

.

But this equation doesn't give very much insight into the actual inner workings of what causes the light to slow down within the material. I'd like to look into that a little further.

When an electromagnetic wave enters a material, the electric field will cause the electrons in the material to oscillate. The disturbance will be proportional to the permittivity of the material. However, the oscillation will be slightly out of phase with the applied electric field. Thus, the charges oscillating will create their own electric field. When all the electric fields are summed, they create an electric field with a wavelength slightly shorter than the wavelength of the applied electric field and the velocity of the electromagnetic wave will be reduced.

If we look back at the real and imaginary parts of the susceptibility for an EIT system that we calculated earlier shown in Figure 3-1, the absorption is associated with the imaginary part (dashed line).
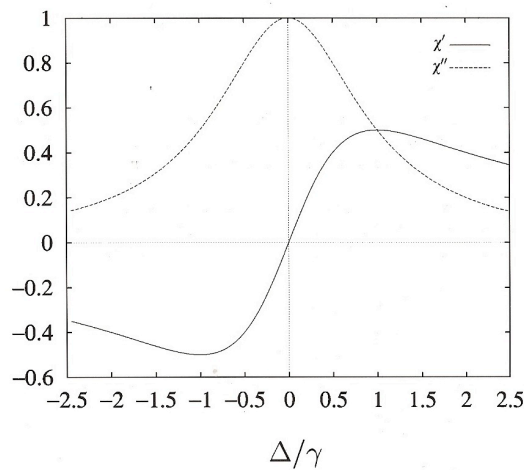
Figure 3-1 Real and imaginary parts of the susceptibility for an EIT system as a function of the detuning.

At zero detuning, there is no absorption – this is what EIT (Electromagnetically induced Transparency) describes. However, the real part of the susceptibility is associated with the dispersion and the index of refraction. At zero detuning, this is also zero, so the index of refraction is unity. But it is clear to see that the derivative is not zero at zero detuning. This creates a large number in the denominator of the index of refraction for the group velocity, as shown by

$$v_g = \frac{c}{n - \omega_p \dfrac{dn}{d\omega_p}}$$

(78)

,

and will make the light slow down even though the index of refraction is unity. For a larger slope in the dispersion curve, the light will slow down even more.

As we discussed earlier, the strength of the coupling beam is responsible for the distance between absorption peaks. And if you consult the graph again, the distance between the absorption peaks roughly corresponds to the width of the linear region in the dispersion curve. Therefore, by decreasing the distance between the absorption peaks by decreasing the coupling beam power, the value of the derivative of the dispersion plot at zero detuning will increase. If this is successfully pulled off, we will be able to vary the speed of the light fairly easily by varying the power of the coupling beam.

4. Packaging Atomic Vapors

We have chosen to use rubidium as the element with which the laser beam will interact and EIT and slow light will be achieved. Rubidium has an appropriate energy structure and has been used before fairly successfully. But it brings along its own set of challenges.

4.1. Rubidium

Rubidium is an element with an atomic number of 37 shown in Figure 4-1. It is a silvery-whitish metal with an a melting point of about 40°C. Thus it doesn't take much heat to melt it. It is among the alkali metals. The alkali metals are notorious for being quite volatile. Rubidium is no exception. The structure of the atom is such that it has only one electron in its valence shell with all the other electron shells either full or empty. It also has one of the lowest electronegativities of any element. As a result, the one valence electron is not bonded very tightly to the nucleus and can move around and react with surrounding atoms readily. Rubidium can be very dangerous and reacts violently to air and water. For this reason, precaution must be taken when working with Rubidium.

In our case, we work with Rubidium in a glove box that has an inert nitrogen atmosphere with less than a 1 in 1 million count of oxygen. We use the glove box to maintain the Rubidium in its usable state as well as protect ourselves from a possibly dangerous situation.

Figure 4-1 Periodic Table

Rubidium reacts with many common elements, partially as a result of its low electronegativity. This will be discussed more thoroughly in the sealing section of this thesis, but for now it is sufficient to say that it is difficult to find materials with which Rubidium will be inert.

Rubidium has two naturally occurring isotopes. About 72.2% of Rubidium is ^{85}Rb, while the remaining 27.8% is ^{87}Rb. The energy transitions that we use for EIT are in ^{87}Rb. Figure 4-2 shows the energy structure of ^{87}Rb along with the wavelengths in nanometers that are associated with the different transitions.

In our experiments, we focus mostly on the D1 and D2 lines. The D1 line corresponds to the transition between $5^2S_{1/2}$ and $5^2P_{1/2}$, which is about 794.8 nm. Similarly, the D2 line corresponds to the transition between $5^2S_{1/2}$ and $5^2P_{3/2}$, which is about 780 nm.

If you recall from section 2.4, in order for EIT to occur, we must have a lambda system. When we factor in the hyperfine lines that the $5^2S_{1/2}$ line splits into (F=1,2). These two energy states become the base of the lambda system, while $5^2P_{1/2}$ or $5^2P_{3/2}$ becomes the peak of the lambda system depending on whether we are using the D1 or D2 line.
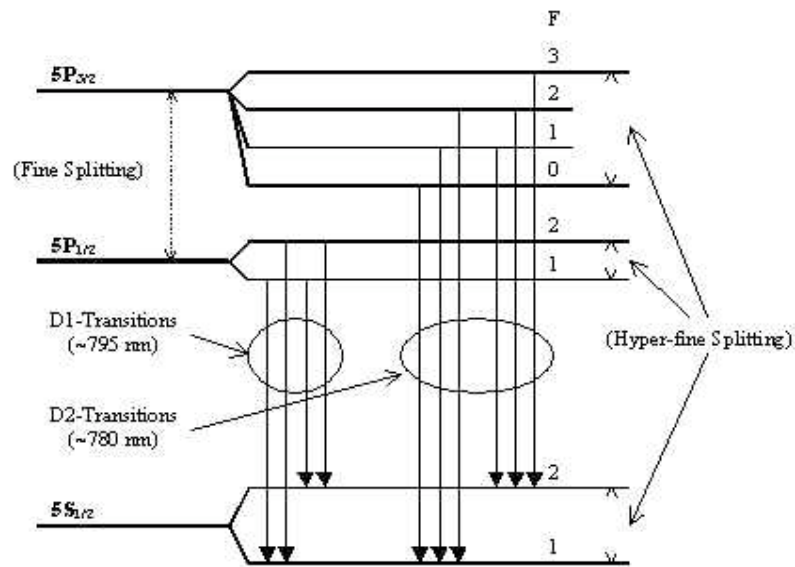
Figure 4-2 Rubidium energy structure (not to scale)

At this point in the thesis, we come to the part that I made a unique contribution to. Since we want to analyze EIT and slow light in Rubidium vapor, we need to first find a way to

introduce Rubidium vapor into the hollow waveguide without it reacting or degrading in any way. At either end of the hollow waveguide there are openings. So somehow these both need to be sealed with Rubidium gas inside the hollow waveguide.

4.2. Sealing Requirements

As part of the process of finding an appropriate sealing method for sealing the copper reservoir for the rubidium vapor onto the silicon chip, we developed a list of requirements that must be fulfilled in order to have a successful seal. These are the most important requirements for any potential sealing method:

First, we must use the present ARROW schematic. While we can add elements, the basic structure must remain the same. The main reason behind this is the pure time and effort that has been put into building up the ARROW platform. This time and effort includes all the recipes for growing the dielectric layers, the masks for the ARROW platform and the expertise that has been build up in making these devices.

Second, we must use something that is nonreactive with rubidium. This seems like a fairly innocuous expectation for a sealing substance, but is harder than it seems. Very few epoxies and other sealing agents have been tested for their compatibility with Rubidium, so it has basically taken a trial and error process to bring us to viable options.

Third, the sealing method must create a hermetic seal to the ARROW platform. This may be obvious, but it's important to point out that without having a good seal, the Rubidium will

react with the air and the device will fail. In order to seal, the sealing agent must be able to form around the three dimensional waveguides and fill in any corners created in the ARROW production process.   This implies that the sealing method have some viscosity that will allow it to flow a bit.

Fourth, the sealing method must create a robust seal. In our collaborative research, all the devices are shipped to Santa Cruz for optical testing. So, in order to ensure that the device arrives in Santa Cruz intact, the seal must be able to withstand some jostles and bumps.

Fifth, the sealing process must not damage the device. Some of the sealing agents that we have considered require high temperatures to set the agents, but the dielectric layers can't handle high temperatures and will crack at those temperatures. The sealing process also must not require any type of mechanical agitation. The hollow wave guides are extremely fragile and will not be able to take any mechanical agitation especially from imprecise human hands holding tools.

Fifth, the sealing agent must have temperature stability up to about 100°C. When we test the device for EIT and slow light, the device is heated up to increase the atomic density of the Rubidium gas in the hollow waveguide. If the seal starts to break down at those higher temperatures, it will defeat the purpose of all that has gone into producing the devices.

We also have adopted some techniques that we'd like to use and incorporate into the final device fabrication process. These are not necessities, but they seem to work and have provided some sort of direction in the hunt for the perfect sealing technique.

First, copper tube reservoirs for the Rubidium. Copper is fortunately inert in the presence of Rubidium. Also, copper tubing is relatively inexpensive and easy to obtain. This however, also creates the challenge of how to seal the copper tubing to the silicon/silicon dioxide substrate.

Second, the copper tubing can be sealed using a crimping method. This will be addressed later in the loading section, but it's easy, effective, and great.

4.3. Loading Process

The rubidium reservoirs are made from stubs of copper tubing. Although in the past we have used 1/8" copper tubing for the stubs, now we use 3/16" copper tubing. This size is small enough so that it fits onto the ARROW platform, but big enough that rubidium can be placed at the bottom of the tube without any problems.

Once the stubs are attached to the ARROW device, and they are ready to be loaded with Rubidium and sent off for testing. The loading process goes somewhat as follows:

First: the inside of the waveguides are coated with n-oxtyldimethyl (dimethylamino) silane (ODMS). ODMS chains coat the inner walls of the waveguides and then will trap any Rubidium atoms that hit the sides of the waveguide. By disallowing the Rubidium atoms from

bouncing off the walls of the waveguide, we are creating the situation for a more coherent gas, and we will be more able to achieve coherence related quantum experiments such as EIT and slow light.

Second: one end of the waveguide is sealed. This will be the end that does not get the Rubidium metal.

Third: the device is loaded into a nitrogen atmosphere glovebox, which is shown in Figure 4-3. With the nitrogen atmosphere, the Rubidium metal will not be able to react with the oxygen found in a normal atmosphere and will not oxidize or have any other chemical reactions before being loaded into the ARROW devices.

Figure 4-3 Glovebox fill with Nitrogen

Fourth: Rubidium metal is loaded into the still unsealed copper tube. We don't need very much Rubidium – a drop is sufficient. The Rubidium is also heated up to allow it to degass a bit.

Fifth: the copper tube is put under vacuum. The vacuum brings the pressure in the copper tube to about 1 mTorr.

Sixth: while the copper tube is under vacuum, a cold welding tool shown in Figure 4-4 is used to seal the end of the copper tube. This tool is very specialized, but works perfectly for our purposes
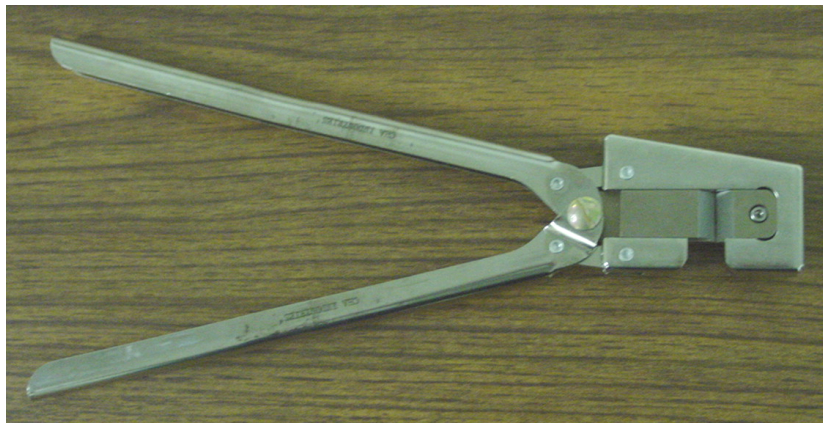
Figure 4-4 Copper Cold Weld Tool

After this process is done, we should have something that looks like Figure 4-5. At this point, the whole device is ready for optical testing and evaluation.

It's important to quickly address some sealing ideas that have been used by other research groups in containing rubidium and to explain why they will not work in this situation.

The group at NIST [36] that made small Rubidium atomic vapor cells used anodic bonding to bond the glass to the wafers. We can't use anodic bonding first of all because of the fragile nature of the waveguides. Also, we need an almost perfectly flat surface to do successful anodic bonding, and the waveguides have a bit of three-dimensionality.
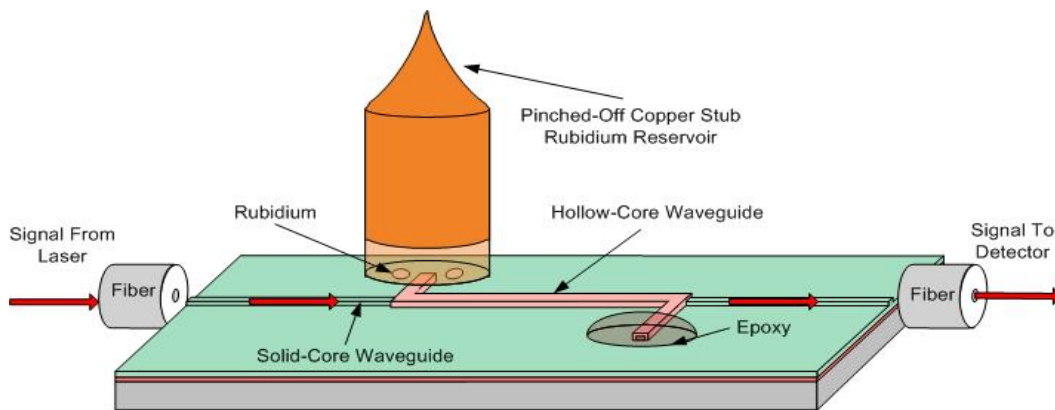
Figure 4-5 ARROW with Rubidium reservoir

In the past, Rubidium atomic vapor cells have been made with complicated glass forming techniques. However, this would not work for our purposes. These glass atomic vapor cells are expensive and complicated to make as well as being much larger than we want. If we were to go towards this method, it would defeat the purpose of all that we've been working towards. The

big advantage of the ARROW platform is that there's potential in integrating it into a larger optical system and that it can be made cheaply. Both of these functions would not be filled by using a glass-formed atomic vapor cell.

4.4. Minicells

The ARROW devices are time and labor intensive to make. With each of those multiple layers, a separate process must be gone through and even when all goes well, there's a chance that only a few of the chips on the die will be functional. But in order to test all of these sealing methods, it's been necessary to find a platform in which we can test the sealing capabilities and the inertness (or lack of) in the presence of Rubidium vapor.

We needed a fast, reliable, robust, inexpensive way of examining each of our sealing methods without actually using the ARROW platform. We also needed a way to optically characterize these prototyping devices. So in order to find a way to test the different sealing methods, we came up with what we call minicells. Minicells provide a simple platform on which we can test our sealing methods while maintaining many similar characteristics of the ARROW platform.

The minicells, as shown in Figure 4-6, are composed of a glass vial, a copper tube, and the material used to seal one to the other. The copper tube is then sealed by crimping it as we do with the ARROW devices. We are able to test for a good seal between the glass vial and the

copper tube by using a vacuum during the loading process. We are then able to test for

Rubidium compatibility by measuring the atomic density of the Rubidium vapor and then

measuring the atomic density after multiple heating and cooling cycles.
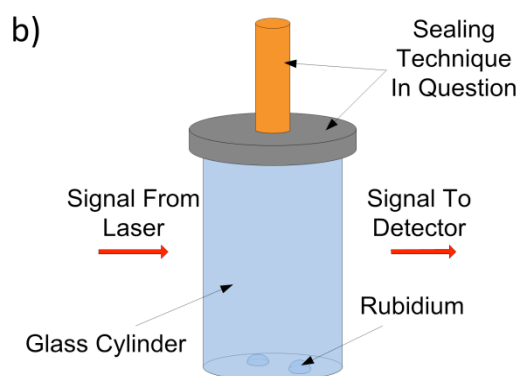
Figure 4-6 Minicell diagram

These minicells act similarly to the bulk cells in that the absorption spectrum of

Rubidium can be measured with them.

The minicells worked great for us for a long time. However, at a certain point, we started

experimenting with sealing methods that required an application of heat. As the minicell is a

three-dimensional device, it was difficult to work with and provide a consistent even application

of heat simultaneously. As a result, we used a variation on the minicell to provide better

Rubidium compatibility data.

4.5. Housekeeper Sealed Minicells

Part of the difficulty involved in finding a good sealing method between copper and glass is the notorious difficulty in attaching metals to ceramics of any sort. Substances that stick to one don't tend to love sticking to the other. And when these substances are found, they generally don't play friendly with Rubidium.

Another problem in the adhesion between copper and glass is the vast difference in the Coefficient of Thermal Expansion (CTE). These differences are shown in Figure 4-7. The Coefficient of Thermal Expansion refers to the percentage of volume change per degree Kelvin change. If the sealing method requires application of heat (and many of them do), then the differences of CTE could very well cause the seal to fail after cooling.

	Coefficient of Thermal Exp
Silicon	3 E-6/K
Copper	17 E-6/K

Figure 4-7 Coefficient of Thermal Expansion for Silicon and Copper

However, the differences in CTE between silicon or glass and copper can be utilized to our benefit. We can use ductile or "housekeeper" seals to create minicells that don't have an additional material between the copper and glass and thus can be used for Rubidium compatibility tests.

The housekeeper seals involve creating a compressive mechanical seal between the copper tube and a glass vial. Since the copper in addition to having a high CTE, has fairly high ductility, it is able to form to the surface of the glass and thus form a high quality strong seal. Figure 4-8 demonstrates the method behind making the housekeeper's seals.
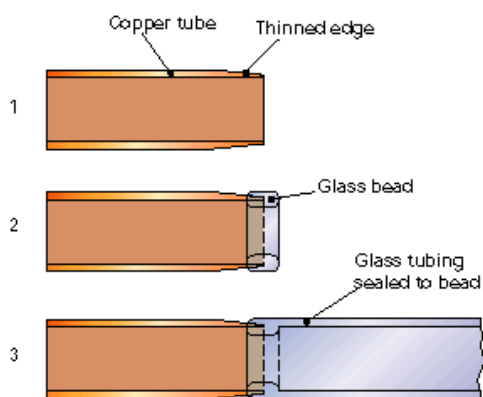
Figure 4-8 Housekeeper seal between copper and glass

When completed, the housekeeper minicells look like Figure 4-9

Figure 4-9 Picture of Housekeeper minicell

As noted, the main advantage to using a housekeeper seal in a mini cell is that now we can eliminate the sealing method and test a variety of substances for nonreactivity with rubidium. Unfortunately, the main disadvantage to the housekeeper minicells is that they are a bit expensive and it becomes prohibitively expensive to test as many substances as we would like. However, by choosing carefully, we were able to test many different substances that would be of interest to know.

The tests were done by loading Rubidium and the substance under inspection into one of these housekeeper minicells under vacuum and then performing some atomic density tests on them. The following graph shows the results of how many common substances reacted and which are possible candidates for being compatible with Rubidium.

Atomic Density % Drop

Materials (x-axis): Empty, Epoxy, Gold, Chrome, Palladium, PMMA, Aluminum, Tin, Nickel, Silicon, Stainless Steel, Brass, Zinc, Silver, Lead, Indium

Material
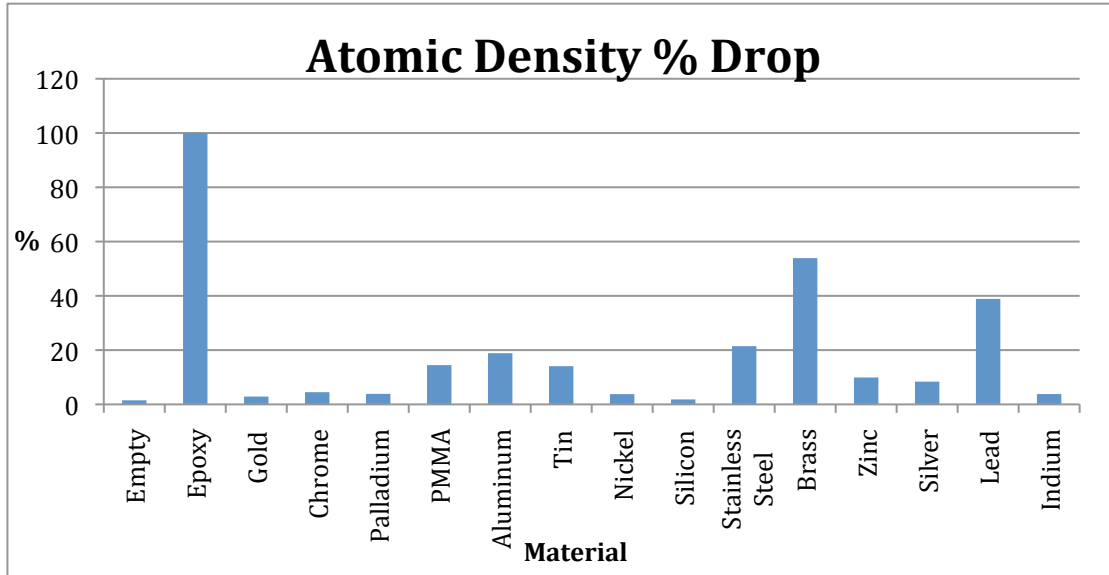
Figure 4-10 Atomic Density percentage drop of various substances in housekeeper minicells.

From Figure 4-10, we can see that the smaller the percent drop the better. This would correspond to a substance that has little reaction with rubidium and thus will be able to maintain a strong seal and the Rubidium gas will last for awhile in its presence.

Some of these materials will be addressed further in the sealing section of this thesis because of their positive showings on this test.

Overall, the housekeeper minicells have been valuable because they have helped us identify useful substances to turn to and work with in our search for a good sealing method for the Rubidium filled ARROW devices.

4.6. Absorption Tests

After the minicells are evacuated, loaded with rubidium, and sealed with the cold welder, they are sent to Santa Cruz for testing. In Santa Cruz, the researchers there test the effectiveness of the sealing method by doing absorption tests on the minicells.
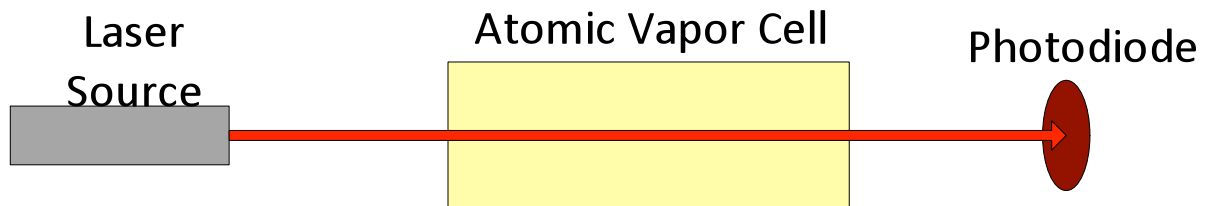
Figure 4-11 Absorption test diagram

These tests were done as shown in Figure 4-11 by measuring the absorption profile of the gas within the heated minicell by shining a tunable laser through the minicell and scanning across the desired frequencies.   If there is a high enough concentration of the atomic vapor, the laser will be absorbed at some frequencies that correspond to the electronic transitions within the atoms in the vapor. This is called the absorption spectrum. A sample spectrum for rubidium is shown in Figure 4-12.

A cell with a high atomic vapor density will show deep ditches in the absorption spectrum at the transition frequencies while a cell with a low atomic vapor density will show very shallow ditches. A high atomic vapor density signifies that the sealing method is effective

and that it does not react much with the rubidium vapor while the opposite signifies an ineffective sealing method.
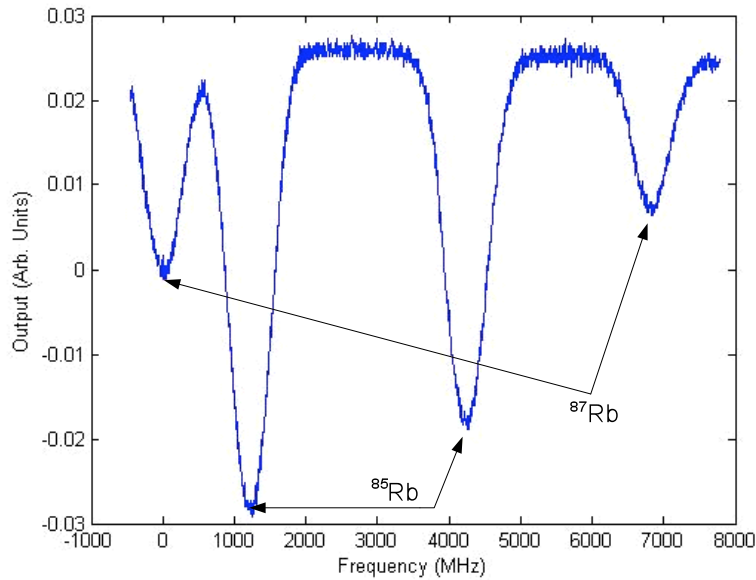
Figure 4-12 Sample absorption spectrum for Rubidium vapor

The atomic density can be measured from the absorption spectrum. Higher atomic densities will correspond to deeper dips in the spectrum while cells with low atomic vapor density with show very shallow ditches. A high atomic vapor density signifies that the sealing method is effective and that it does not react much with the rubidium vapor, while the opposite signifies an ineffective sealing method.

$$P_{out} = P_{in}e^{N\cdot\sigma_{ij}\cdot L} \tag{79}$$

is used to calculate the actual atomic density. In this equation N corresponds to the atomic density, σ_{ij} is the cross section corresponding to that particular transition, L is the interaction length and P_{in} and P_{out} are the Power in and out respectively. The results from these minicell tests for the individual sealing methods will be addressed in the sealing method section of this thesis.

5. On Chip Sealing Procedures

5.1. Sealing Methods

5.1.1. Mounting Equipment

In order to make mounting the copper stubs onto the silicon chips with ARROW waveguides more consistent and take out as much user error as possible, we developed some mounting devices designed to hold the copper stub in position while the sealing material is drying/cooling/solidifying.

First up is the room temperature mounting blocks. These mounting blocks involve an aluminum clip that has been attached to a thick copper wire. The copper wire is in turn attached to some sort of focusing mechanism. These have been designed so that the copper stub can be raised or lowered depending on what is needed. The copper wire allows the operator to adjust the angle at which the copper tube is secured. We have two separate room temperature mounting blocks. One is shown in Figure 5-1.

These mounting blocks work well for any mounting process done at room temperature. Each of the stubs can have the sealing material on its end. This can then be adjusted so the end of the copper tube is parallel to the surface of the chip and the stub can then be lowered until there is good contact between the stub and the chip. After letting this sit for the desired amount of time, the sealing material will have cured and be ready for testing.

75

A problem arises, however when it is necessary for heat to be applied to the sealing material. The room temperature mounting blocks are mostly made of metal and thus act as large heat sinks. This isn't practical for a material that needs to be quite hot to seal effectively. We also run into problems when the sealing material requires some sort of mechanical agitation to achieve an effective seal as there is no way to move the stub once it has been placed in the clip in the room temperature mounting block. These two problems have been solved by using our heated mounting block.
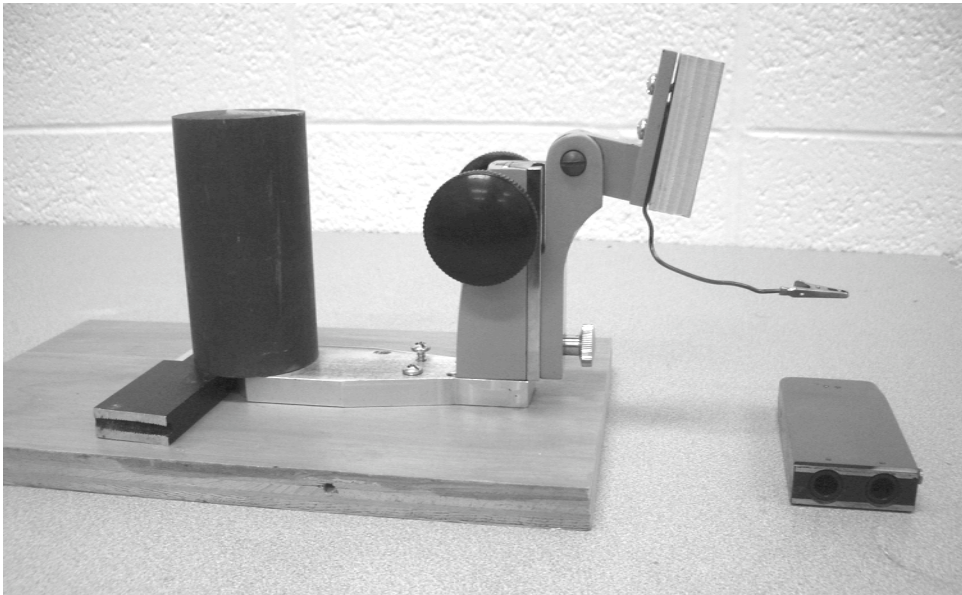
Figure 5-1 Room Temperature mounting block. The silicon chip will go on the grey block, while the copper stub will be held in the clip and adjusted with the wire connected to the clip.

In reality, the heated mounting block is a drill press and a hot plate, but it performs its job quite effectively. The hot plate provides a constant source of heat and we can fairly accurately control the temperature of the chip. The drill press also provides the lowering and rising control

of the copper stub that we had when using the room temperature mounting block. The heat sink effect is also overcome by using a Teflon stub holder that is put into the drill press chuck so that in essence the chip and the copper tube are the only elements that are heated up. The drill press also is able to rotate the chuck, so when mechanical agitation is necessary, it is definitely possible.

The one drawback to using the drill press is that it is impossible to change the angle of the incidence of the end of the copper stub onto the silicon chip. However, this can be overcome by ensuring that the end of the copper tube is perpendicular to the length of the copper tube. This is illustrated in Figure 5-2
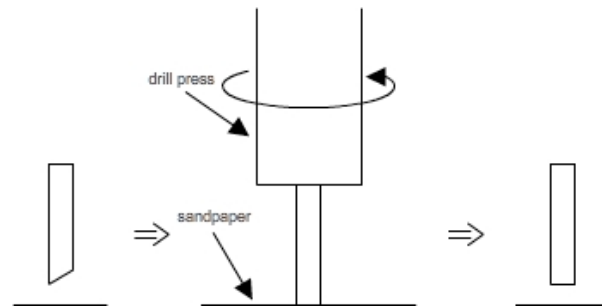
Figure 5-2 Crooked copper tubes can be straightened with a drill press and sandpaper

We can make the copper tube perpendicular to its length by using another drill press to sand the end of the copper tube. It's necessary for us to sand down the end of the copper tubes regardless because the cutting process to make them short enough doesn't leave the end smooth or regular enough. But when I'm trying to make the end of the tube perpendicular to its length, I

place the tube in the chuck of a drill press as if it were a drill bit. I then place a piece of sand paper underneath the chuck and run the drill press at a low speed. This gives a nice, smooth surface that will work in the heated mounting block.

The following methods use one of these two types of mounting blocks, although there are slight variations of which mention will be made.

5.2. PMMA

Based on its ready availability and its decent showing on the housekeeper minicell tests, PMMA (Plexiglas) was tried in the sealing tests. We actually tried two methods of applying the PMMA in an attempt of finding an appropriate sealing method.

5.2.1. Procedure

We got the thinnest PMMA we could find—0.031 inch thick. From the PMMA small donut-shaped pieces were cut with a laser cutter. These donuts corresponded to the size of the copper tubes used for the reservoirs—about 3/16 inch outer diameter and 1/8 inch inner diameter.

The PMMA donut was placed with the donut hole over the opening of the hollow waveguide. This was in turn placed directly under the stub in the heated mounting block. The

chip and PMMA were heated to the desired temperature. The stub was lowered onto the PMMA

donut. The whole system was allowed to cool. The end result is shown in Figure 5-3.
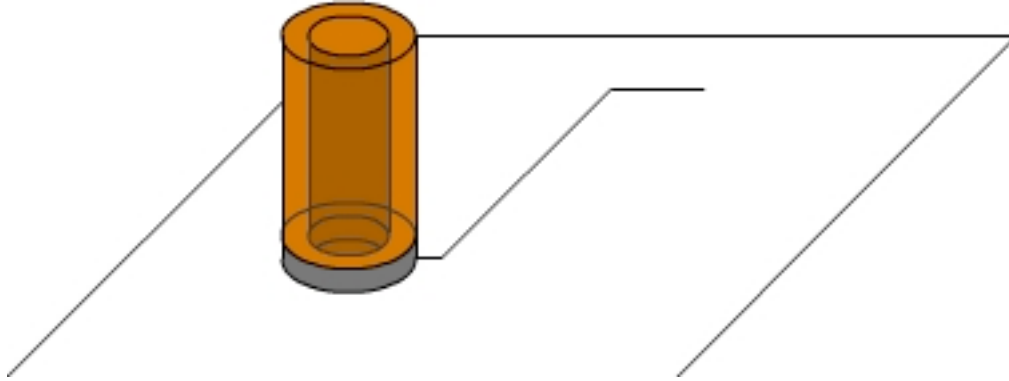
Figure 5-3 PMMA donut between copper stub and silicon substrate

Alternately, with the second PMMA application method, a piece of PMMA was placed in

a beaker with some acetone in it. Acetone dissolves PMMA, so after a few hours in the acetone,

the PMMA had dissolved, and I had a goopy concoction. This could be applied to the end of a

stub and then lowered down in the appropriate position onto the silicon chip.

5.2.2. PMMA Results

Ultimately, both of these applications were rejected for the following reasons:

When using the first method, we encountered problems in the actual sealing method.

Depending on the temperature the device was raised to, the PMMA acted differently. When the

device was only raised to slightly higher than 160°C, which is the melting point of PMMA, the

PMMA itself maintained its pristine transparency and didn't appear to have any substantial chemical changes, but the seal between the copper tube and the silicon substrate was not hermetic as well as being quite fragile. Because of the absence of a good seal, we were forced to abandon this process.

The same process was attempted with the device being raised to about 190°C and even higher. At these temperatures, the PMMA started to bubble and change colors to a caramel color. The sealing at these higher temperatures was inconsistent, probably because of the bubbles in the PMMA. Sometimes the device seemed to seal well, but other times, it did not have an acceptable seal. This higher temperature process was abandoned as well.

The alternative process of PMMA with acetone also ran into snags. When I made a minicell sealed with this material, the minicell successfully sealed and a vacuum was created in it. However, shortly after the Rubidium was loaded into the cell, the rubidium turned bright blue. It was clear that even though the PMMA had solidified because much of the acetone had evaporated, some molecules from the acetone were left behind and the rubidium reacted with them. It was immediately clear that this wasn't the ideal sealing material and this approach was abandoned.

5.3. Crystal Wax

Crystal wax is a wax that is sometimes used in cleanroom processes to mount devices for processing. This seemed especially interesting and promising because as was mentioned earlier, bulk atomic vapor cells are often coated on the inside with paraffin to keep rubidium atoms from bouncing off the walls. The crystal wax seemed to have a similar chemical makeup to paraffin and thus seemed like a good candidate for sealing.

5.3.1. Procedure
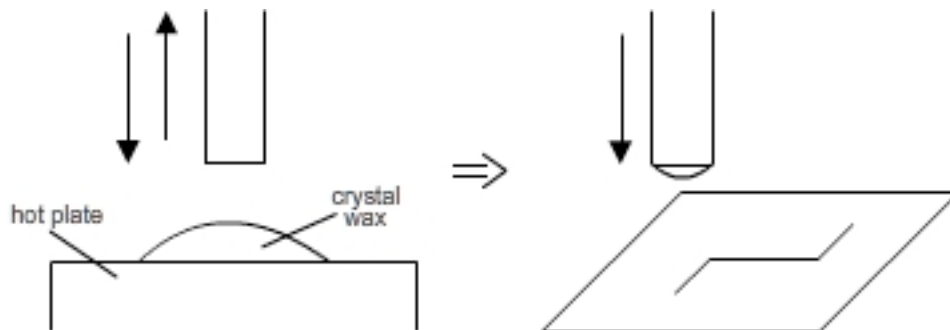
Figure 5-4 Crystal wax is applied to the end of a copper tube and then the copper tube is applied to the ARROW device

A small piece of crystal wax was melted on a microscope slide. The copper tube mounted in the drill press was lowered down into the melted crystal wax. The copper tube was

then lowered onto the silicon chip. The entire device was then allowed to cool. This procedure is shown in Figure 5-4.

5.3.2. Crystal Wax Results

A few problems arose with the crystal wax attachment method. First of all, when the chip with the attached stub was inspected it was found that the crystal wax had wicked along the channel past the corner and almost halfway along the main channel length as illustrated in Figure 5-5.
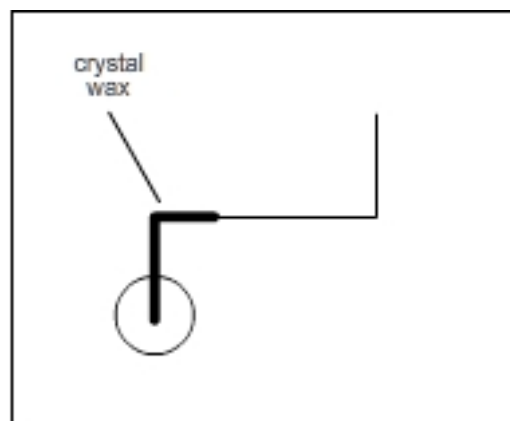
Figure 5-5 Crystal wax wicks along waveguide

The wicking was caused by capillary action and would effectively prevent the waveguide from guiding light because the addition of another substance right around the waveguide regardless of the index of refraction ruins the waveguide that was addressed earlier in the thesis.

Also, when we made minicells with a crystal wax seal, and loaded Rubidium into them. The Rubidium had undergone a chemical reaction by the next day. This effectively concluded any additional research into crystal wax sealing. The crystal wax seemed inappropriate for use with waveguides and Rubidium and likely wouldn't work for sealing these ARROW devices.

5.4. Cerasolzer/S-Bond

In an attempt to find a suitable sealing material, many thorough internet searches were made. Among these searches, we found solders that claimed to have the ability to seal glass to metal. There were two general brands of these glass to metal solders: Cerasolzer and S-Bond. Although these two brands have solders of slightly different compositions, they have similar sealing mechanisms.

According to Cerasolzer literature, each of the solders contains a small amount of elements such as Zinc, Tin, Silicon, Aluminum, Beryllium, and Rare Earth metals. These elements all have a strong chemical affinity with oxygen. During the bonding process, they will react with the oxygen in the air to form an oxide, which then is chemically bound to the surface of glass, ceramics, metal oxide, etc. The bonding process seems to occur at the liquid-solid reaction between the oxides themselves. Figure 5-6 shows the hypothesized bonding mechanism between the Cerasolzer solder and the substrate.
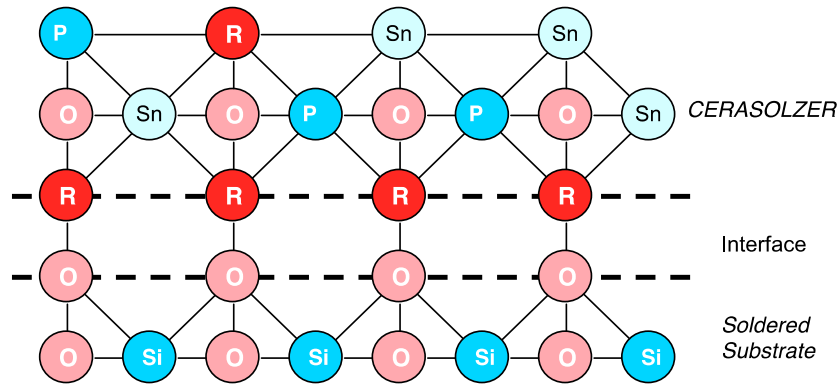
Figure 5-6 Diagram for Cerasolzer bonding mechanism. R signifies the metal oxides

The other requirement in the sealing process was some kind of mechanical agitation of the sealing surface in order to break some of the O-H bonds so that the oxygen atom on the surface of the substrate would be able to react with the metal oxides and would bond to them. This is effective. When there's a proper amount of agitation, the stub will seal to the silicon chip and create a strong joint. However, when the solder and the sealing surface were agitated effectively, the hollow waveguides would be broken. Essentially, in order to create a good seal, every part of the sealing substrate needed to be scratched with some kind of tool. This was impossible to do by hand without breaking the waveguide

At this point, we ordered a new tool to help with the Cerasolzer attachment—an ultrasonic soldering iron. The ultrasonic soldering iron is designed to help solder without the addition of flux. So it seemed ideal for our purposes. An example of our ultrasonic soldering iron is shown in Figure 5-7.

Figure 5-7 Ultrasonic Soldering Iron

The ultrasonic soldering iron works by sending ultrasonic pulses into the molten solder. It's essential that there's an outside source of heat to both of the surfaces being soldered to ensure that the solder is actually molten. The ultrasonic pulses perform a few different functions. First: the ultrasonic energy breaks down the cohesion within the solder and thus reduces the surface tension. This will let the solder flow more readily. Second: the ultrasonic energy breaks the oxygen bonds on the substrate and allows those oxygen atoms to react with the metal oxides in the solder. Third: the ultrasonic energy forces the solder into cracks, crannies, and crevices to make a stronger joint. This process is shown in Figure 5-8.
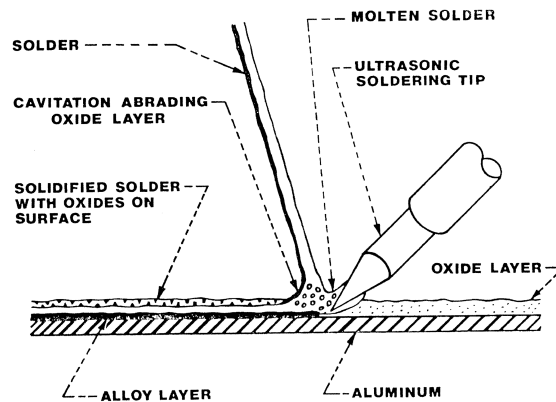
Figure 5-8 Application of active solder with the ultrasonic soldering iron

5.4.1. Procedure

Donuts of Serasolzer solder are cut out of the Serasolzer solder foil with two standard

hole punches found at a local craft store. A 1/8" hole is punched followed by a 3/16" hole to

create a donut shape. A donut of Cerasolzer solder is placed in the desired location with the

donut hole directly over the opening to the hollow waveguide. The entire chip is placed on the

hotplate in the heated mounting block. A copper tube that has previously had solder applied to

one end with the ultrasonic soldering iron is placed in the Teflon holder. The chip is heated up

past the heating point of the solder which varies depending on which solder allow is being used.

The ultrasonic iron is used with the flat side of the iron towards the chip. This is lightly drawn

over the face of the chip where the solder is desired. After the solder is applied to the chip, the

copper stub is lowered to the silicon chip. In order to ensure that the copper stub is hot enough

to melt the solder, I wait for about a half hour at this point.
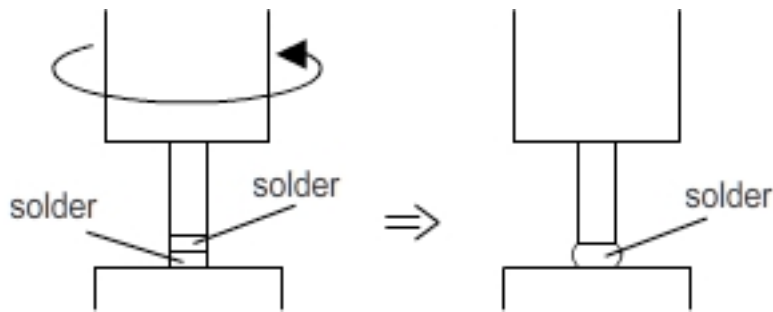
Figure 5-9 the oxide between the two masses of solder must be broken by rotating the drill press chuck.

After the half hour has passed, I break the surface oxide on the chip and the stub by

rotating the stub. This is possible because the heated mounting block is simply a drill press.

This rotation breaks the surface oxide of the solder and allows the solder from the chip and the

stub to flow together. This process is shown in Figure 5-9

5.4.2. Cerasolzer/S-Bond Results

The ultrasonic soldering iron works surprisingly well. It is exceedingly rare to find

something that will directly bond metal and glass together, and it's gratifying to see. This would

be useful for any type of bonding that didn't have fragile structures. However, in this case we do

have fragile structures that regardless of how gentle we were with them, the hollow waveguides

in the ARROW device still broke under the influence of the ultrasonic soldering iron. There was always either a break in the hollow waveguides or a leaky seal.

Although the Cerasolzer and S-bond at first appeared to be perfect candidates for the sealing material, upon further investigation we found that although the were quite good at sealing glass and metal together, the sealing process was not gentle enough for our application and thus we needed to find another sealing method.

5.5. Epoxy

It would be difficult to list the many epoxies that have been tried in this hunt for a proper sealing material. Pretty much everything from your basic five-minute epoxy to UV-cured epoxy to high temperature epoxies and everything in between. The major issue in the hunt for an appropriate epoxy for this purpose is that there's a significant dearth of information of what is reactant with rubidium and what is not. In general, epoxy companies do not do those types of tests. Thus we were relegated to trying to find those epoxies that claimed to be fairly non reactive in general and to simply trying out a bunch of different epoxies.

In general, all of these epoxies were tested by building minicells with them, loading rubidium, and then sending them through multiple heating-cooling cycles and watching how the atomic density inside the minicell changed as a result of the heating-cooling cycles.

Some of the epoxies reacted with the rubidium almost immediately. We were able to see a discernable change in the appearance of the rubidium inside the minicell. Whereas pure Rubidium is a silvery-white color, in the presence of different epoxies, the Rubidium turned blue, yellow, black, or developed different sheens on its surface. The epoxies that didn't have any visible effect on the Rubidium were sent to Santa Cruz for the heating-cooling testing.
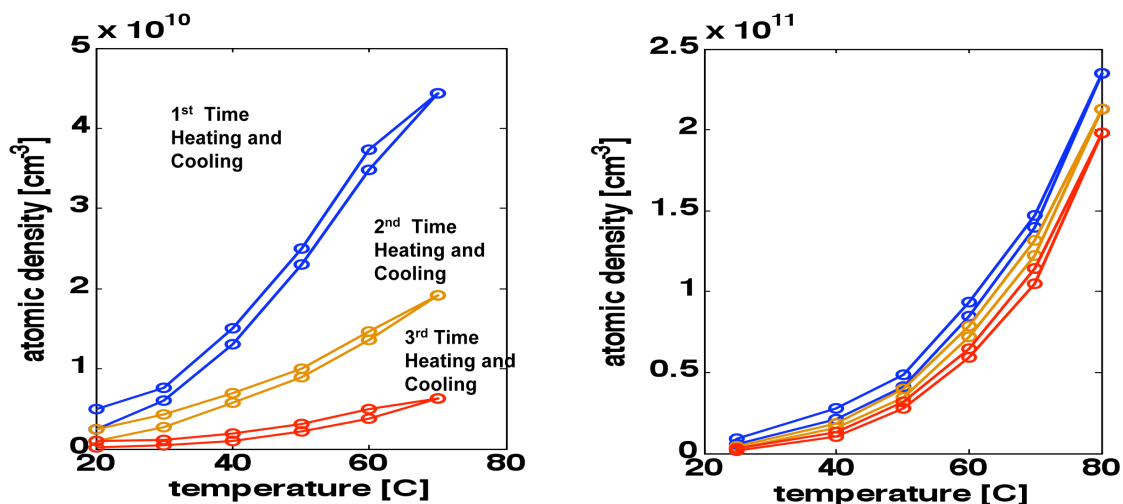
Figure 5-10 Atomic densities in minicells sealed with Low Temperature (Left) vs High Temperature (Right) epoxies

Figure 5-10 illustrates the difference between two different epoxies, a high temperature epoxy and a low temperature epoxy. The graph shows the drop in atomic density within the minicell as a function of the temperature. It also shows the gradual or not so gradual drop of the atomic density through multiple cycles.

In the end the best epoxy that we have found is Aremco 2310. It out performs all of the alternative epoxies that we have tested. However, it is still not perfect. If you look at the previous graph, there is still some reaction between the Rubidium and the Aremco 2310, which is shown by the drop in atomic density over the multiple heating cooling cycles.

5.5.2. Epoxy Procedure

Aremco 2310 comes in two parts that are mixed together in roughly a 50/50 ratio. A small amount of the two parts are mixed together on a glass slide. This is placed on a hotplate preheated to 65°C. It is cooked for 7 minutes and then a very small amount is applied to the end of a copper tube. The copper tube is then placed one of the room temperature mounting blocks. The wire holder is adjusted so the end of the copper tube is parallel to the surface of the silicon chip. Figure 5-11 shows how this is done by eye—looking at the stub at eye level from one direction then turning it 90 degrees and looking again. This is one significant advantage to the room temperature mounting block.

Once the stub is aligned properly and in the right location, it is NOT immediately

lowered onto the chip. Instead I wait until the epoxy that is still on the glass slide has solidified

somewhat. It should be able to "hold a dent" for a few seconds before oozing back into place.

Once the epoxy has reached that point, the stub is lowered to the silicon chip. This is then

allowed to set over night. The chip is then dehydrate baked, but it can't dehydrate bake at the

standard temperature of 150°C because the epoxy wicks along the channel and seals up the

channel when heated to that temperature. Instead, the dehydrate bake is only at 110°C for about

two hours.
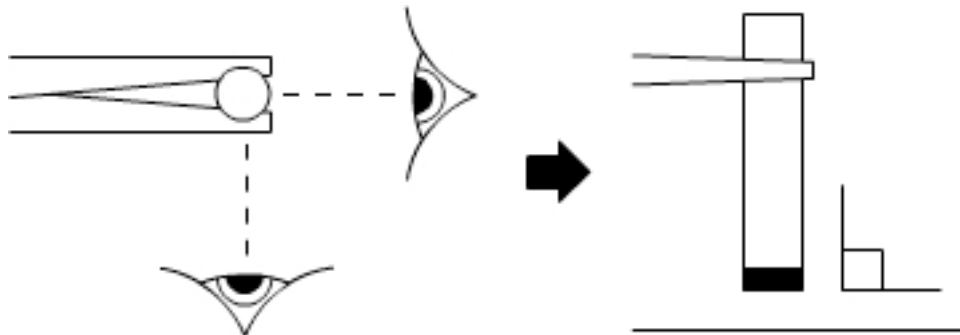
Figure 5-11 To verify the end of the copper stub is parallel to the silicon chip, make sure you look from two different directions.

The working chips that have exhibited EIT and slow light were all manufactured with

Aremco 2310 as the sealing element between the silicon chip and the copper stub. These results

will be addressed later in this thesis. However, these chips failed after only about an hour of

operation. In order to understand the capacity for these chips to withstand high temperatures for extended periods of time, we placed minicells sealed with epoxy in different temperatures. The atomic density of these minicells were tested at specific intervals and the point at which the cells failed was determined. Figure 5-12 shows some extrapolated data from these tests. The It shows the relationship between the temperature the cells are kept and the number of days before failure occurs.   The trend is clear that the minicells kept at high temperatures failed much sooner than those kept at low temperatures. It's difficult to see how many days those cells kept at the higher temperatures lasted, but to clarify, the cell kept at 90°C failed at 4 days, 80°C failed at 8 days, and 70°C failed at 16 days.
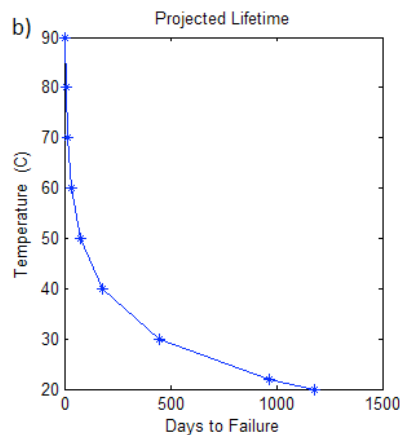
Figure 5-12 Lifetime of minicells sealed with epoxy at different temperatures.

Clearly, the higher the temperature, the sooner the cell fails. Unfortunately, it turns out that the EIT and slow light tests happen when the cell is heated up to 90°C, so it's clear from this graph that they will fail quickly, which we saw in practice.

Although the Aremco 2310 is the most successful sealing agent that we have found, there are some major problems with its short lifetime in the presence of Rubidium. We have also had extremely limited yields of working chips with the epoxy seal. We believe that the parts of the epoxy will separate from the rest and will wick along the ARRROW channels both outside and in. This can easily ruin the guiding capabilities of the ARROWs and make them unusable for our purposes. Clearly we need to come up with another alternative for sealing the reservoirs to the hollow waveguides in the ARROW devices.

5.6. Indium Solder

If we refer back to the Atomic density drop chart (Figure 5-13) done in the housekeeper minicells, we obviously were drawn to materials that had the lowest density drop as we thought they'd be the best possible candidates for non reactive sealing materials. From among the those, Indium stuck out for a few reasons.

Atomic Density % Drop
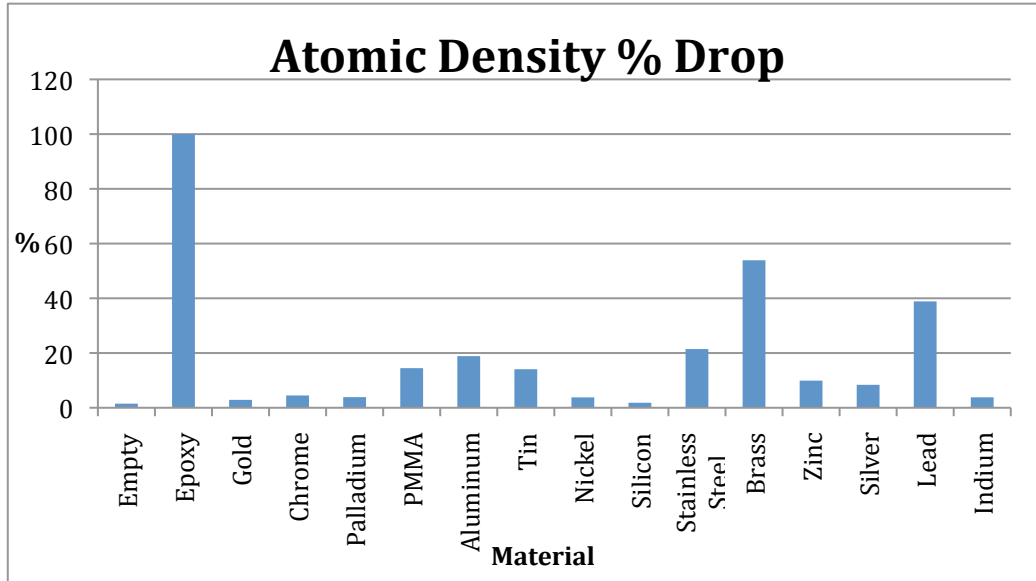
Figure 5-13 Atomic density percentage drop for different substances measured in housekeeper cells.

First: Indium has a very low melting point of 156°C. This puts it in the realm of realistic temperatures that wouldn't damage the ARROW PECVD layers. Very few pure elements have that low of a melting point.

Second: Indium has the interesting characteristic of being able to wet to glass. This takes a bit of effort and some mechanical agitation, which as we found when looking at the Cerasolzer solder makes it a challenge to use with the ARROW devices, but the wetting ability could be used for us.

Third: Using pure indium would be awesome because the fewer elements there are in the sealing material, the fewer elements there are to react with the Rubidium and cause problems.

But the Indium would not work on it's own because of the need for mechanical agitation. However, the Indium Corporation sells a flux that can be used to attach Indium and Nickel. After consulting with them, we came up with a new addition to the ARROW platform. Donut-shaped regions of chrome and nickel would be placed over the openings to the hollow core waveguides. These would be used as soldering sites for the copper stubs. The chrome is necessary to promote adhesion between the nickel and the Silicon Oxide. On the opposite side of the solder joint, the ends of the copper tubes were also coated with chrome followed by nickel, because even though indium and copper will bond to each other, the allow they create is quite brittle, and the indium-nickel bond is much stronger. This was all necessarily done in the electron beam evaporator in the cleanroom here at Brigham Young University. The following figure illustrates the ARROW platform with the new soldering sites. The donuts are designed so that either 1/8" or 3/16" copper tubing could be used.

5.6.1. Procedure

Indium is a very soft metal. For this reason, I can cut off small pieces of Indium wire with a razor blade. These small pieces are placed on the soldering site. Another characteristic that comes along with Indium being a soft metal is that when the small pieces of indium are picked up with tweezers they often stick to one of the prongs of the tweezers. When the piece of indium is lightly touched to the silicon surface it will stay where it is placed.

Previously the copper stub had chrome and nickel deposited on its end. Figure 5-14 shows how the copper stub is placed on the tip of a generic soldering iron, which is clamped with its tip pointing up. The soldering iron heats up quite quickly, so the copper stub is ready for indium within a few minutes. Small pieces of indium are placed on the tip of the heated copper stub. At this point it's easiest to use indium that has a flat edge as the circular wire pieces tend to fall off the copper tub onto the soldering iron. When a piece of indium is situated on the tip of the copper tube, a very small amount of flux is added. Thus far I have used the wooden end of a cotton swab to dip in to the flux and to place a small amount of flux onto the end of the copper tube. This will cause the indium to wet to the nickel coating. Another small piece of indium is placed followed by a small amount of flux and this is repeated until there is a ring of indium on the tip of the copper tube. The copper tube is then allowed to cool.

It's important that only small amounts of flux are used. If too much is use, the flux will remove some of the metal deposited on the copper and the indium will not simply wet to the metal coating without some other means of encouragement. If this occurs, and often it does as it is hard to control the indium and flux on this scale. I have had success with using the ultrasonic soldering iron to ensure that there is good adhesion of the indium to the metals deposited on the stub. It's gratifying to be able to use that equipment even if its for an entirely different purpose than was originally meant. The ultrasonic soldering iron can help the indium adhere to sections of the copper where the flux has eaten away some of the deposited layers.

At this point, we're able to put these two pieces together, Figure 5-15 shows howthe copper tube is situated over the soldering site without touching the indium on the silicon chip. The chip is heated up to 235°C . When it has heated up and the indium has melted, little chunks of indium on the surface of the silicon will acquire a slightly different sheen and any corners will soften. It will be clear that the indium is liquid, although it will maintain it's shape quite well. When the indium is melted, the copper tube is lowered down onto the beads of melted indium. This will cause the indium to solidify from the cool copper tube. In order to let the entire copper tube heat up sufficiently, I let the entire system heat for about half an hour.
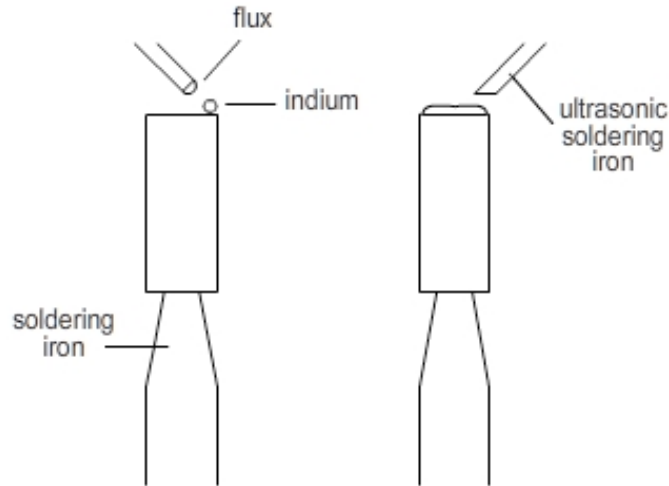
Figure 5-14 Indium is put on the copper stub by placing a small piece of indium on the heated copper and adding a small amount of flux. This is then repeated until the end of the copper stub is completely covered.

At the end of the half hour, I lower the copper tube down until it's almost touching the silicon surface. At this point, I'm ready to add a drop of flux. The flux will flow around the tube. I try to not add so much flux that it wicks over to the other nickel donut as the donut will likely not be useable for future soldering if it's exposed to flux as the flux removes some of the metal coating. The whole device is allowed to cool.

At this point, it's necessary to remove the flux that has solidified around the joint and often wicked into the hollow waveguide channel. The flux can be removed by a 3 hour soak in fairly concentrated soapy water. We use a simple soap called Alconox, which is used in the cleanroom. If the concentration of the soap in the water is not high enough, there is a white residue left behind that will ruin any guiding of the waveguides. In order to clean the soap from the channel, the entire device is soaked in DI water overnight. Once this is done, the device is rinsed off, dried, and ready for loading.
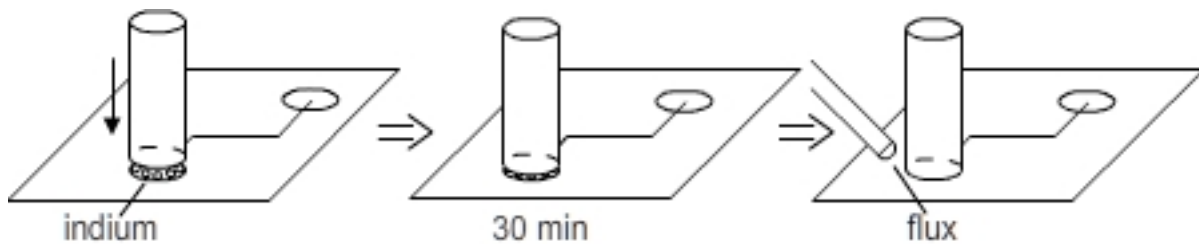
Figure 5-15 Small pieces of indium are placed at soldering site, and heated. The copper stub is lowered onto the Indium pieces, heated for ½ hour, then flux is added.
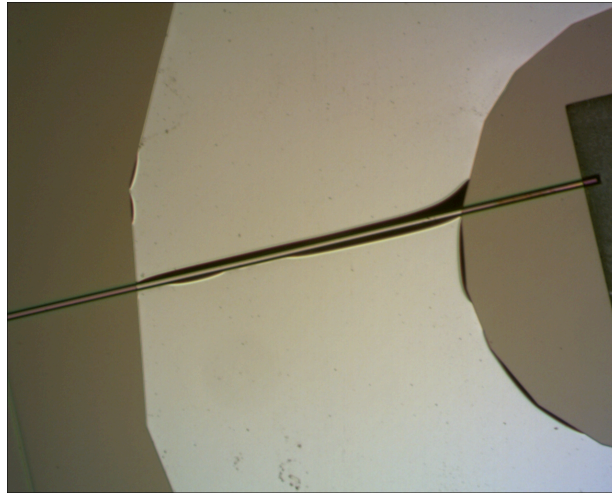
Figure 5-16 Chrome Nickel Donut on dielectric and silicon substrate. The poor adhesion around the channel is clearly visible.

So far, the real issue that we have faced with these devices is that we have had difficulties in getting consistent sealing. When we looked at this closer, we looked at the indium-chrome donuts deposited on the silicon wafer. Many of them looked like what is shown in Figure 5-16.

The adhesion is often poor because of the difficulty in depositing metals onto sides of features. The e-beam evaporator has the capabilities to do partially isotropic deposition because of its rotating planetary element, but the depositition is still fairly directional as shown in Figure 5-17. Often the layers on the sides of features have difficulties adhering and have high stress so they peel off easily

chrome / nickel

5µm
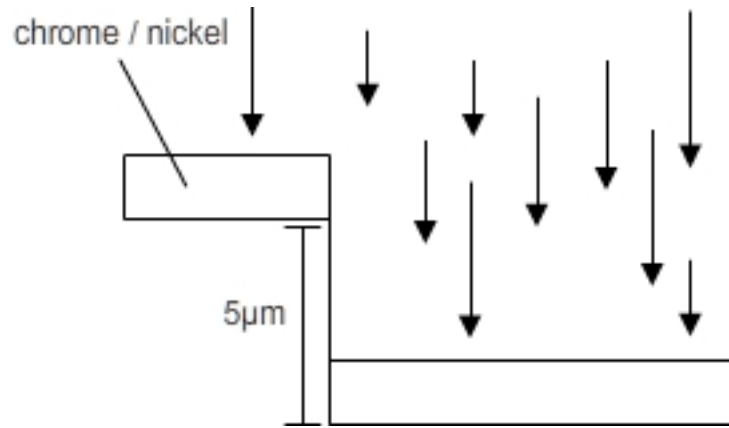
Figure 5-17 It's difficult to get good adhesion along the walls of the waveguide due to the directional nature of the e-beam evaporator

Thus far in this research, the indium sealing method seems to be the most promising and has the potential to allow us to build devices that are non reactive to rubidium and will last for extended periods of time and allow us to perform more extensive experiments on them and potentially use these devices in commercial products.

6. On Chip Results

All that has been addressed thus far in this thesis has been leading up to these results—the actual demonstration of Electromagnetically Induced Transparency (EIT) in a Rubidium-filled ARROW device and then the associated slow light measurement on the same device.

This was accomplished in an ARROW device that had a copper tube sealed to one end of the hollow waveguide, with the other opening sealed with a small drop of epoxy. The inside of the hollow waveguide was coated with ODMS. A small amount of Rubidium was placed inside the copper tube reservoir. The reservoir was evacuated and sealed by crimping the copper tube. The whole device was sent to our colleagues at the University of California Santa Cruz for testing.

After verifying that the device maintained its light guiding properties, they used the set up shown in Figure 6-1 to test for EIT.

In this setup, light from two tunable External Cavity Diode Lasers with Rabi frequencies of Ω_c(coupling laser), and Ω_p(probe laser) respectively are coupled together into a single mode optical fiber, the light is passed through an isolator and then the optical which is end-coupled to the solid core section of the ARROW platform. The light which passes through the Rubidium

vapor filled hollow core is collected by an objective lens and passed to a photo detector. The

signal can be collected and analyzed from that point.
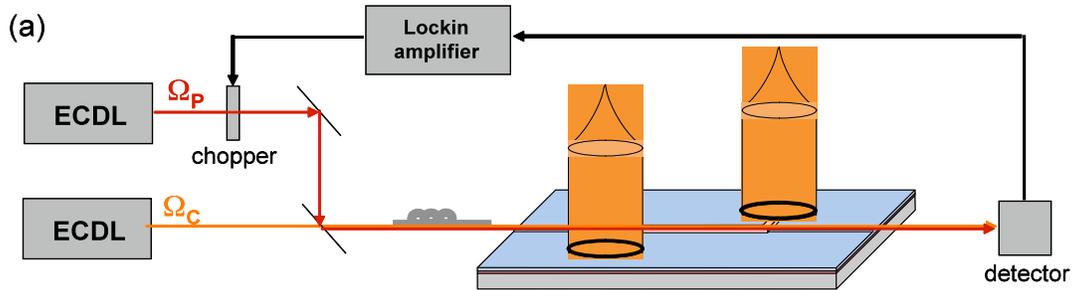
Figure 6-1 Setup for EIT experiment

The coupling laser is locked into the $(5S_{1/2},F=3)$->$(5P_{3/2},F=3)$ transition in ^{85}Rb. The

probe laser, on the other hand is modulated at a frequency of 1 kHz by an optical chopper and

tuned around the $(5S_{1/2},F=2)$->$(5P_{3/2},F=3)$ transition in ^{85}Rb.

Figures 6-2 and 6-3 show the results of this test. These graphs show the transmission of

the probe laser through the Rubidium filled hollow waveguide first without any coupling beam

applied and then with the coupling beam at full power. We can clearly see that without the

coupling beam, the curve looks like a standard absorption curve. However, when the coupling

beam is applied, we see an increase in transmission of the probe beam at exactly the $(5S_{1/2},F=2)$-

>$(5P_{3/2},F=3)$ transition. In this case, we were able to recover 44% of the transmission at the

frequency corresponding to the transition mentioned above. While not the perfect transparency

that EIT predicts, the difference is clear to see. These graphs illustrate that it is possible to get

EIT, however imperfect it might be, in a chip-based device such as the ARROW platform.
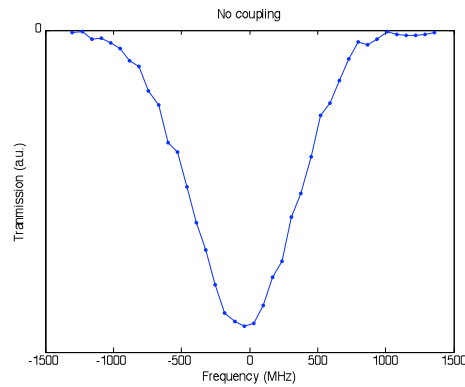
Figure 6-2 Transmission around D1 line with coupling beam turned off
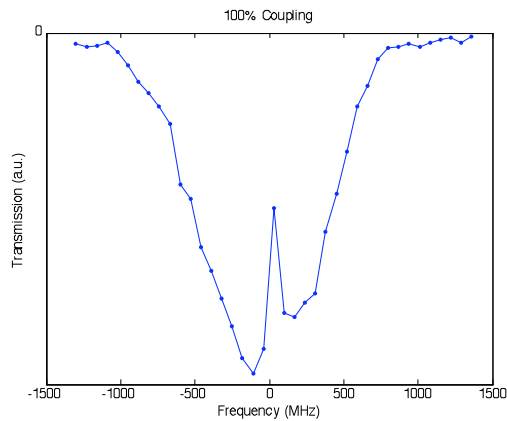
Figure 6-3 Transmission around D1 line with coupling beam at 100%
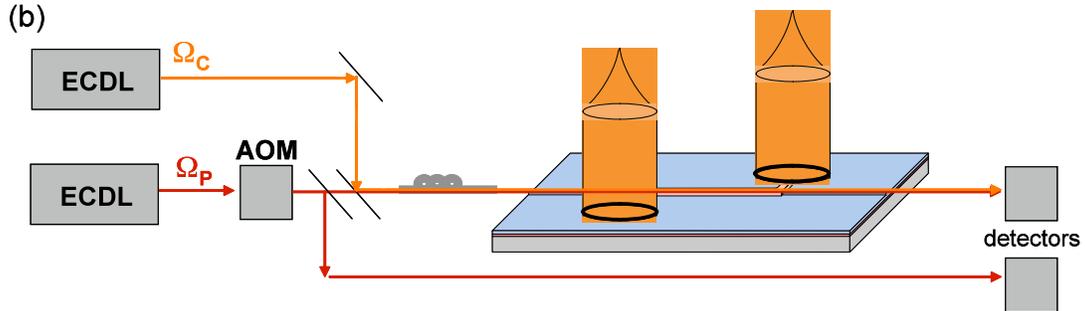
Figure 6-4 Experiment setup for Slow Light experiment

Once EIT was achieved, the tests for Slow Light involved a very similar setup with only a few variations shown in Figure 6-4. Once again, there are two tunable External Cavity Laser Diodes with Rabi Frequencies Ω_c(coupling laser), and Ω_p(probe laser) respectively. These are coupled together through an isolator into the ARROW device. However, the difference comes because in order to see a change in the velocity of light, we need to see one pulse traveling slower than the other. The probe laser was modulated by an acousto-optic modulator (AOM) to create 20ns long pulses repeated at a rate of 5 MHz. The probe laser was split so that some of the light traveled through the Rubidium vapor in the ARROW wave guide while some of the light bypassed the ARROW and simply propagated through the air. Each of these beams of light was detected by a different detector and then the difference in traveling times was calculated. Through this method, the velocity of the light through the atomic vapor could be calculated. Because of the reasons that we discussed earlier in the thesis, the group velocity of the pulse

should that travels through the Rubidium vapor should be significantly smaller than that of the pulse that travels through air.

When the pulses are compared, the Figure 6-5 is obtained. The circles correspond to the pulse that traveled through air, while the squares correspond to the pulse that traveled through the ARROW device. It's clear that the latter pulse arrived at the detector after the former pulse and thus had a smaller group velocity. This particular measurement shows the first demonstration of slow light through quantum state control on a chip.
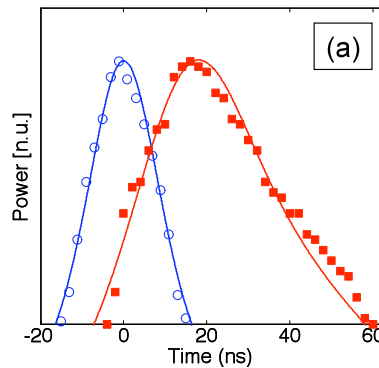
Figure 6-5 In slow light experiment, the circles signify beam that propagated through ambient air, squares show beam that propagated through Rubidium vapor

This same measurement was repeated for multiple coupling powers and as expected for a smaller coupling power, the group velocity decreased. Just as a reminder of why this is expected, let's go back to the EIT energy structure. When the coupling beam is applied it

essentially splits the top energy level in two. A stronger coupling beam will force those two energy levels farther apart. This comparison is shown in Figure 6-6. With a weak coupling beam, the two energies will be close together. This corresponds to a bandwidth in which the absorption changes drastically. And thus, the steeper that the index of refraction curve will be. Therefore, a weaker coupling beam will correspond to slower light.

Figure 6-7 describes the relationship between the coupling laser power and the group velocity on the left hand of the graph and the relationship between the coupling laser power and the group index of refraction on the right hand of the graph. The lower limit of this particular experiment shows that we were able to decrease the group velocity from 3.0×10^8 m/s (the speed of light in a vacuum) to 2.5×10^5 m/s. This is a drastic difference. It definitely demonstrates the capacity that the ARROW platform has for these quantum coherence applications.
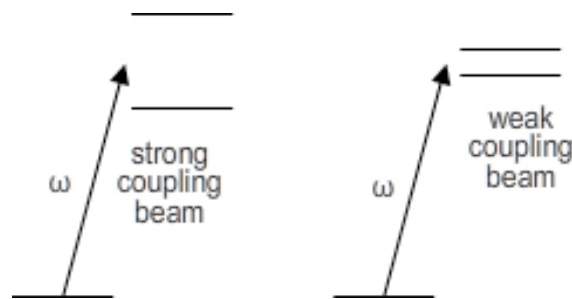
Figure 6-6 A strong coupling beam pushes the split levels apart, a weak coupling beam keeps the levels closer together.

The major downside in this particular device was that at the temperatures required for creating enough rubidium within the hollow waveguide caused the rubidium to react with the epoxy seal. As a result, this device only exhibited EIT for about an hour. Although there were many other experiments we would have liked to perform on the device, there was simply not enough time to do those. This is the crux behind the search for a better sealing method. The goal is to be able to create devices that are stable and thus will be much more useful in commercial applications and we will be able to perform many more experiments on them.
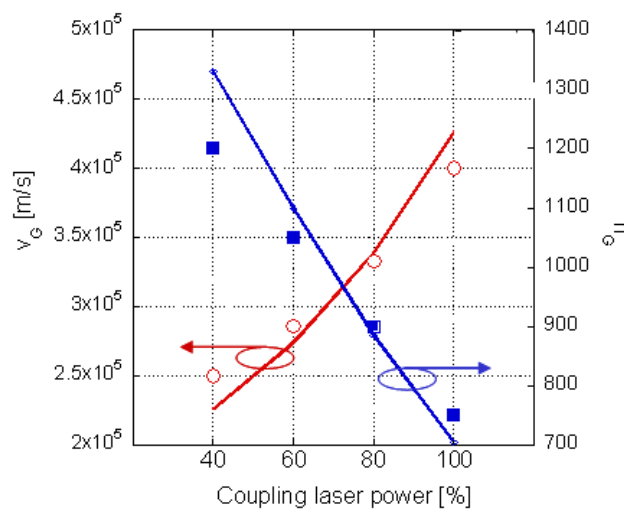
Figure 6-7 Lower coupling laser power leads to lower group velocity of light

This is the first demonstration of slow light in a chip based system. We believe as we perfect the sealing methods and build better ARROW systems, we will be able to achieve even slower light and do other quantum optic experiments using this platform.

7. Conclusion

In conclusion, this thesis has detailed the process and research behind achieving the first on chip EIT and slow light results through a novel technique involving hollow core optical waveguides.

In the past, many researchers have been able to achieve both EIT and slow light in bulk atomic vapor cells. In an attempt to miniaturize this process and make it more feasible in commercial instruments we have been using a platform of Anti Resonant Reflecting Optical Waveguides (ARROW) devices to both guide light and contain the interacting matter. However, the platform creates a whole new set of challenges when integrating rubidium vapor into the hollow waveguides as rubidium is highly reactive and it is difficult to maintain an inert atmosphere for the rubidium vapor.

The sealing method for containing the rubidium vapor has several requirements: it must be compatible with the ARROW platform; it must be non-reactive with rubidium vapor; it must create a hermetic seal; it must be stable up to 100°; and it must be a gentle method that doesn't damage the ARROW device.

A variety of sealing methods were attempted and their fulfillment of the previous requirements was analyzed. Among these sealing methods were PMMA, Crystal Wax, Active Solder, Epoxy, and Indium Solder. PMMA, Crystal Wax and Active Solder each had major

faults in one or more of the sealing requirements. We have used a high temperature epoxy with relative success to contain the rubidium vapor. However, the epoxy degrades very quickly at the high temperatures required for EIT testing. Indium solder is the most recent application method. It has high potential although we have yet to fully test its effectiveness.

We were able to successfully demonstrate the first EIT and slow light on a chip with our ARROW atomic vapor cell system. In the slow light experiment, we were able to slow light down to 2.5×10^5 m/s. The group velocity of light decreased from the standard 3×10^8 m/s by a factor of 1200. We believe we can achieve even lower group velocities using this same platform through further experimentation.

In the future, we would like to take these new stable ARROW based atomic vapor cells and do some further slow light tests and even perform stopped light tests where the data contained in the optical pulse is temporarily stored within the rubidium atoms. We'd also like to do more quantum optic experiments including but not limited to four wave mixing, entangled photon generation and other nonlinear optical tests. This gives us a lot of hope for the future of integrated optics as the concepts that we've learned and perfected could be applied to other platforms other than the ARROW platform. These platforms could potentially be integrated into commercial devices for use in optical buffers, single photon emitters, and other optical devices.

REFERENCES

[1]   Alzetta, G., Gozzini, A., Moi, L., Orriols, G., Nuovo Cimento B **36**, 5 (1976)

[2]   Kocharovskaya, O.A., Khanin, Y. I., Sov. Phys. JETP **63**, 945 (1986)

[3]   Gornyi, M. B., Matisov, B. G., Rozhdestvenskii, Yu. V., Sov. Phys. JETP **68**, 728 (1989)

[4]   Kocharovskaya, O. A., Khanin, Y. I., Sov. Phys. JETP Lett. **48**, 630 (1988)

[5]   Harris, S. E., 'Lasers without inversion: interference of lifetime-broadened resonances.' Phys. Rev. Lett. **62**, 1033 (1989)

[6]   Scully, M. O., Zhu, S-Y., Gavridiles, A., 'Degenerate quantum-beat laser: Lasing without inversion and inversion without lasing.' Phys. Rev. Lett. **62**, 2813 (1989)

[7]   Imamoglu, A., Harris, S. E., 'Lasers without inversion: interference of dressed lifetime-broadened states.' Opt. Lett. **14**, 1344 (1989)

[8]   Boller, K.-J., Imamoglu, A., Harris, S. E., 'Observation of electromagnetically induced transparency.' *Phys. Rev. Lett*. **66**, 2593 (1991)

[9]   Field, J. E., Hahn, K. H., Harris, S. E., 'Observation of electromagnetically induced transparency in collisionally broadened lead vapor.' Phys. Rev. Lett. **67**, 3062

[10]   Harris, S. E., 1997, 'Electromagnetically induced transparency', *Phys. Today*, June, 36.

[11]   Fleischhauer, M., Imamoglu, A., Marangos, J. P., 2005, 'Electromagnetically induced transparency: Optics in coherent media', *Rev. Mod. Phys.,* **77**, 633

[12]   Marangos, J. P., 1998, 'Topical review Electromagnetically induced transparency', *J. Mod. Optics*, **45**, 471

[13]   Bigelow, M. S., Lepeshkin, N. N., Boyd, R. W., 'Superluminal and slow light propagation in a room-temperature solid.' *Science* **301**, 200 (2003)

[14]   Hau, L. V., Harris, S. E., Dutton, Z., Behroozi, C. H., 'Light speed reduction to 17 metres per second in an ultracold atomic gas.' *Nature* **397**, 594 (1999)

[15]   Lukin, M. D. 'Colloquium: Trapping and manipulating photon states in atomic ensembles.' *Rev. Mod. Phys.* **75**, 457 (2003)

[16]   Kasapi, A., Jain, M., Yin, G. Y., Harris, S. E., 'Electromagnetically induced transparency: propagation dynamics.' *Phys. Rev. Lett.* **74**, 2447 (1995)

[17]   Camacho, R. M., Pack, M. V., Howell, J. C., 'Wide-bandwidth, tunable, multiple-pulse-width optical delays using slow light in Cesium vapor.' *Phys Rev. Lett.* **98**, 153601 (2007)

[18]   Notomi, M., Kuramochi, E., Tanabe, T., 'Large-scale arrays of ultrahigh-Q coupled nanocavities.' *Nature Photonics* **2**, 741-747 (2008)

[19]   Baba, T., 'Slow light in photonic crystals.' *Nature Photonics*, **2**, 465-473 (2008)

[20]   Vlasov, Y. A., O'Boyle, M., Hamann, H. F., McNab, S. J., 'Active control of slow light on a chip with photonic crystal waveguides.' *Nature* **438**, 65 (2005)

[21]   Ghosh, S., Bhagwat, A. R., Renshaw, C. K., Goth, S., Gaeta, A., 'Nonlinear optical interactions with rubidium atoms confined in a hollow-core photonic crystal fiber' Quantum Electronics and Laser Science Conference (QELS) May 21, 2006

[22]   Xia, F., Sekaric, L., Vlasov, Y., 'Ultracompact optical buffers on a silicon chip.' *Nature Photonics* **1**, 65-71 (2006)

[23]   Okawachi, Y., Bigelow, M. S., Sharping, J. E., Zhu, Z. M., Schweinsber, A., Gauthier, D.J., Boyd, R. W., Gaeta, A. L., 'Tunable all-optical delays via Billouin slow light in an optical fiber.' *Phys. Rev. Lett.* **94**, 153902 (2005)

[24]   Schmidt, H., Imamoglu, A., 'Giant Kerr nonlinearities using electromagnetically induced transparency.' *Optics Letters*, **21**, 1936 (1996)

[25]   Braje, D. A., Balic, V., Yin, G. Y., Harris, S. E., 'Low-light-level nonlinear optics with slow light.' *Phys. Rev. A.* **68**, 041801(R) (2003)

[26]   Zhang, J., Hernandez, G., Zhu, Y., 'All-optical switching at ultralow light levels.' *Optics Letters* **32**, 1317 (2007)

[27]   Dawes, A. M. C., 'Optical Switching with cold atoms' *Physics* **2**, 41 (2009)

[28]   Phillips, D. F., Fleischhauer, A., Mair, A., Walsworth, R. L., 'Storage of light in atomic vapor.' *Phys. Rev. Lett.* **86**, 783 (2001)

[29]   Vudyasetu, P. K., Caacho, R. M., Howell, J. C., 'Storage and retrieval of multimode transverse images in hot atomic rubidium vapor.' *Phys. Rev. Lett.* **100** 123903 (2008)

[30] Bajcsy, M., Hofferberth, S., Balic, V., Peyronel, T., Hafezi, M., Zibrov, A. S., Vuletic, V., Lukin M. D., 'Efficient all-optical switching using slow light within a hollow fiber.' *Phys. Rev. Lett.* **102**, 203902 (2009)

[31] Light, P. S., Benabid, F., Gouny, F., Maric, M. Luiten, A. N. 'Electromagnetically induced transparency in Rb-filled coated hollow-core photonic crystal fiber.' *Opt. Lett.* **32**, 1323 (2007)

[32] Londero, P., Venkataraman, V., Bhagwat, A. R., Slepkov, A. D., Gaeta, A. L. 'Ultralow-power four-wave mixing with Rb in a hollow-core photonic band-gap fiber.' *Phys Rev. Lett.*

[33] Yang, W., Conkey, D. B., Wu, B., Yin, D., Hawkins, A. R., Schmidt, H., 'Atomic spectroscopy on a chip.' *Nature Photonics* **1**, 331 (2007)

[34] Wu, B., Hulbert, J. F., Lunt, E. J., Hurd, K., Hawkins, A. R., Schmidt, H., 'Slow light on a chip via atomic quantum state control.' *Nature Photonics* **4** 776 (2010)

[35] Klein, M., Novikova, I., Phillips, D. F., Walsworth, R. L., 'Slow light in paraffin coated Rb vapor cells.' *J. Modern Optics* **53** 2583(2006)

[36] Schwindt, P., Knappe, S., Shah, V., Holbert, L., Kitching, J., Liew, L., Moreland, J., 'Chip-scale atomic magnetometer.' *App. Phys. Lett.* **27** (2004)

[37] Perez, M. A., Nguyen, U., Knappe, S., Donley, E. A., Kitching, J., Shkel, A. M., 'Rubidium vapor cell with integrated Bragg reflectors for compact atomic MEMS.' *Sensors and Actuators A: Physical* **154** 295 (2009)

[38] Eklund, E. J., Shkel, A. M., Knappe, S., Donley, E., Kitching, J., 'Glass-blown spherical microcells for chip-scale atomic devices' *Sensors and Actuators A: Physical* **143** 175 (2008)

[39] Bajcsy, M., Hofferberth, S., Balic, V., Peyronel, T., Hafezi, M., Zibrov, A. S., Vuletic, V., Lukin, M. D., 'Efficient all-optical switching using slow light within a hollow fiber.' *Phys. Rev. Lett.* **102** 203902 (2009)

[40] Scully, M. O., Zubairy, M. S., <u>Quantum Optics</u> Cambridge University Press 1997

[41] Yin, D., Schmidt, H., Barber, J. P., Hawkins, A. R., 'Integrated ARROW waveguides with hollow cores.' *Optics Express*, **12** 2710 (2004)

[42] Yin, D., Barber, J. P., Hawkins, A. R., Schmidt, H., 'Waveguide loss optimization in hollow-core ARROW waveguides.' *Optics Express*, **13** 9331, (2005)